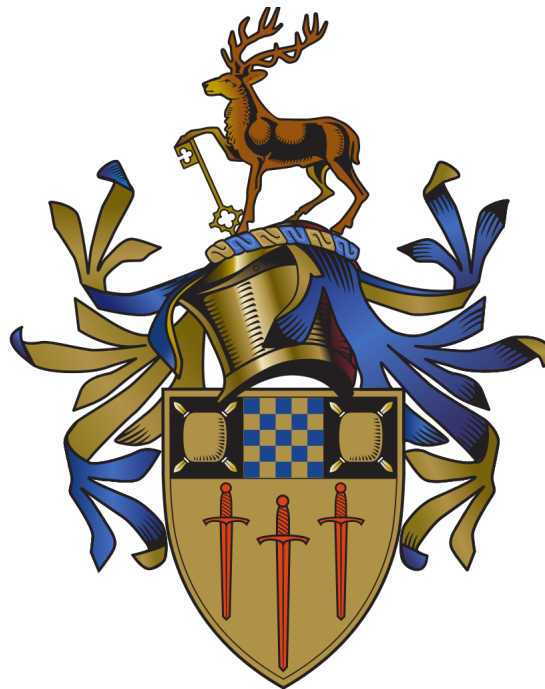


UNIVERSITY OF SURREY

DANG and the Background
Characterisation of HFIR for
PROSPECT



by

Brennan Hackett

A dissertation submitted to the Physics Department in partial
fulfilment of the degree of Master of Physics

January 2017

UNIVERSITY OF SURREY

Abstract

This work is a detailed report on the composition, operation, and findings of DANG, constructed to characterize the reactor-related radiation flux at ORNL's HFIR in preparation for the future short baseline neutrino experiment, PROSPECT. The PROSPECT experiment aims to provide a precise measurement of the antineutrino flux and energy spectrum by taking multiple measurements 7-12 m from the core with a highly segmented ^6Li -doped liquid scintillator detector. These precise measurements will help resolve anomalies observed in reactor-based short baseline experiments' data. Low background rates inside the PROSPECT detector are critical for extracting the needed antineutrino signal, as antineutrinos have a small interaction cross-section. PROSPECT's close proximity to the reactor core makes this is particularly challenging as the reactor produces large amounts of radiation.

Additionally a description of the development and instrumentation used to compose DANG, highlighting its unique design benefits and it's future opportunities with PROSPECT and reactor studies, is given. Different methods used to test and characterise the 17 detectors attached to the array are presented, providing insight into potential effects and challenges one can encounter when building a multi-type detector array.

Furthermore, data collected with DANG has been used to identify potential sources of background radiation creating fluctuations in radiation fields throughout the experimental hall. This work goes on to outline the cause of these sources, discusses their strength and concludes how best to mitigate them. This study also provides information about the spatial and temporal fluctuations in the experimental hall's radiation field PROSPECT will occupy, as well as provide feedback on shielding designs within the hall to further reduce background radiation.

Acknowledgements

I would like to send my deep appreciation to all of my colleagues who helped me complete this project. A special thank you to Elisa Romero-Romero for her help and support getting me started at Oak Ridge and continued aid through the completion of this work. Thank you to James Matta for his support and aid in the data analysis and electrical systems, as well as his feedback on the designs and contrived tests which helped make DANG a reality.

Another big thank you to Blaine Heffron for his effort providing computational support for not only the measurements done with DANG but also with other detectors, furthering my progress towards the completed project. I am even more grateful for his tireless support and patience with me; from teaching me detector systems and neutrino physics to providing entertaining company during long hours spent collecting data at HFIR.

I would also like to recognize all the engineers and scientists at HFIR and in the PROSPECT collaboration, without whom this current project would never have come to fruition. A special thank you to David Glasgow for producing the radioactive sources used through out the work and Geoffrey Deichert for answering endless questions about reactor operations and functions.

Thank you to Becca for her support and patience as I wrote my thesis, my experience at ORNL would have simply not have been as fulfilling or enjoyable without you. Thank you as well to Pat for the kindness and help given over this past year, I am indebted to you for so many hours of your encouragement and support. Additionally, thank you to Armando for his thoughts and edits.

I would also like to extended a special thanks to Paul Stevenson for answering my many last minute emails pertaining to my project and providing his ongoing support throughout my research placement.

Finally, a sincerely special thank you to my adviser and mentor; Alfredo Galindo-Uribarri. The opportunities and guidance he has provided me through out my placement have cultivated a previously unknown love for experimental physics. My decision to continue onto a PhD is largely contributed to the inspiration he has sparked in me over the past year. His tireless hours guiding me with great enthusiasm not only helped keep me motivated but truly made this project a very memorable and enjoyable experience.

Contents

Abstract	i
Acknowledgements	ii
List of Figures	v
List of Tables	vii
1 Introduction	1
1.1 Reactors	2
2 Motivation	4
2.1 Fission	4
2.1.1 Fission Yields and Energy	5
2.1.2 Decay Paths	6
2.2 Reactor Neutrinos	7
2.2.1 Neutrino Detection	7
2.2.2 Reactor Antineutrino Anomalies	9
2.3 PROSPECT Experiment	10
2.3.1 PROSPECT at HFIR	11
3 Radiation Detection	14
3.1 Gamma-ray Interactions	15
3.2 Scintillation Detectors	17
3.2.1 Sodium Iodide NaI(Tl) detector	18
3.2.2 Cerium Bromide CeBr ₃ detector	18
3.3 Neutron Interactions	19
3.3.1 Fast Neutron Detectors, NE213 Liquid Scintillator	20
3.3.2 Slow Neutron Detectors, ³ He Proportional Counter	22
3.4 Pulse Shape Analysis	23
3.4.1 Digitizers	24
3.4.2 Pulse Shape Discrimination	25
4 Detector Array to measure Neutron and Gamma-rays: DANG	26
4.1 Detectors	27

4.1.1	Sodium Iodide Detectors (NaI(Tl))	28
4.1.2	CeBr ₃ Detector	33
4.1.3	NE213 Detectors	35
4.1.4	³ He Tube Detectors	37
4.2	Electronics	39
4.2.1	CAEN VX1730 Digitizer	40
5	Background Measurements	44
5.1	Aims of Survey	44
5.2	Method of Measurement	45
5.2.1	Reactor Status	45
5.3	Temporal Study	46
5.3.1	NaI(Tl) Results	46
5.3.2	CeBr ₃ Results	50
5.3.3	³ He Results	51
5.3.4	NE213 Results	53
5.4	Spatial Study	54
5.4.1	NaI Results	56
5.4.1.1	Reactor On Scan	57
5.4.1.2	Reactor Off Scan	58
5.4.2	³ He Results	60
5.4.2.1	Reactor On Scan	60
5.4.2.2	Reactor-Off Scan	60
5.5	Simulations	61
6	Outlook and Summary	64
6.1	Conclusions of Background Characterisation	64
6.2	Future work	65
	Bibliography	67

List of Figures

1.1	Graphite reactor at Clinton laboratories, now referred to Oak Ridge National Laboratory.	3
1.2	Image of reactor pool inside HFIR.	3
2.1	Fission yields of various fuel sources	6
2.2	Decay back to stability following $^{235}\text{U} + n$ fission.	7
2.3	Anitneutrino flux measured at Daya-Bay	8
2.4	IBD interaction using ^6Li -doped scintillator	9
2.5	Daya-Bay antineutrino spectrum	10
2.6	PROSPECT's location at HFIR	11
2.7	PROSPECT detector layout at HFIR	13
3.1	γ -ray interactions with matter	15
3.2	A γ -ray interacting with an orbital electron	16
3.3	Spectrum comparing CeBr ₃ detector with other crystals	19
3.4	PSD on an electronic pulse	21
3.5	Diagram of ^3He tube	22
3.6	Cross-section as a function of energy for $n(^3\text{He},p)$	23
3.7	Neutron capture cross-section for various proportional counters	24
4.1	Size comparison between DANG and PROSPECT	27
4.2	Detector positions on DANG	28
4.3	^{207}Bi energy spectrum from NaI(Tl) detector	29
4.4	NaI(Tl) γ -ray spectrum taken for reactor on/off	30
4.5	Rate versus gain for a NaI(Tl) detector.	31
4.6	FWHM energy resolution as a percentage versus the energy of the gamma peak measured. These measurements were all taken with the same NaI(Tl) detector.	32
4.7	CeBr ₃ spectrum taken during reactor-on	34
4.8	Image illustrating location of CeBr ₃ detector on DANG	34
4.9	Pulse taken from the CeBr ₃ detector. Evidence of small ringing can be seen in the tail of the pulse.	35
4.10	Image of a NE213 fast neutron detector.	36
4.11	Neutron-gamma discrimination plot collected from a AmBe source.	37
4.12	NE213 spectrum while the reactor was running.	38
4.13	^3He energy spectrum diagram	39
4.14	Pulse from a ^3He tube detector.	40
4.15	DANG: highlighting electronics for the ^3He tubes.	41

4.16	DANG: highlighting the polyethylene moderating material on the ^3He counter.	41
4.17	DANG: highlighting the MPOD HV supply and the mobile support structure.	42
4.18	Digitizer resolution as a function of rate.	42
4.19	Dang: highlighting the digitizer and patch panel.	43
5.1	NaI(Tl) spectrum comparing reactor-on and reactor-off	47
5.2	Rates in a NaI(Tl) detector from a reactor on period.	48
5.3	Rates in detectors during HB-3 Exp 556	49
5.4	Rates in a NaI(Tl) detector from a reactor off period.	50
5.5	Rates in a CeBr ₃ detector from a reactor off period.	51
5.6	Rates in a ^3He counter from a reactor on period.	52
5.7	Rates in a NE213 detector from a reactor on period.	54
5.8	Floor plan of HFIR with future PROSPECT site highlighted	55
5.9	1-3 MeV γ -ray intensity as a function of position at HFIR; reactor on. . .	56
5.10	3-5 MeV γ -ray intensity as a function of position at HFIR; reactor on. . .	57
5.11	1-3 MeV γ -ray intensity as a function of position at HFIR; reactor off. . .	58
5.12	3-5 MeV γ -ray intensity as a function of position at HFIR; reactor off. . .	59
5.13	^3He counter intensity as a function of position at HFIR; reactor on.	60
5.14	^3He counter intensity as a function of position at HFIR; reactor off.	61
5.15	Measured versus simulated γ -ray data from a reactor on period.	62
5.16	MIF background contribution, measured and simulated.	63

List of Tables

3.1	Energy resolution for various scintillators	19
4.1	Intrinsic efficiency and resolution for DANG's NAI(Tl) detectors	32
4.2	Rate correction factors for NaI(Tl) detectors.	33
5.1	Simulated IBD-like rates in a PROSPECT 20 litre cell	62

*Dedicated to my beloved DANG, through the thick and thin you
stood strong and helped me along. . .*

Chapter 1

Introduction

Neutrinos are considered to be the second most common elementary particle in the universe, following closely behind the Photon[1]. However, despite their extremely prevalent nature, describing their properties has proven to be a formidable challenge for physics. This is largely due to the neutrinos elusive nature, being able to travel through enormous distances in matter without interacting even once[2]. Nevertheless, understanding the fundamental details of these prevalent particles has direct implications on our understanding of the standard model and fundamental interactions in nature.

As described by the standard model, neutrinos are left-handed leptons and therefore interact by the weak force[2]. Neutrinos can fall into three different lepton families: e , μ and τ . Since neutrinos have only been seen to interact under the weak force, they displayed tendencies of being a massless particle with further evidence that the lepton number is strictly conserved.

The discovery of neutrino oscillations in the 1990's, however, disproved these assumptions and highlighted gaps of knowledge in the standard model. The fact that neutrinos can oscillate demonstrates that they have a mass and that lepton number is not strictly conserved[2]. This was one of the first instances where the standard model was proven to be incomplete.

Strong sources of neutrinos are important for studying neutrino oscillations and their behaviors due to their large penetrating power. There are many sources of neutrinos, such as cosmogenic, but well understood and controlled sources are needed so that the measurements can be clearly comprehended. Reactors are human-controllable sources of neutrinos. The large number of β^- decays in the neutron rich fission fragments results in a rich number of neutrinos being produced. As well, the fission process has been relatively well understood and characterised for many years. Reactors are ideal for

studying neutrinos, and neutrinos therefore become ideal radiation to study reactors, again due to their large penetrating power.

Currently the neutrino's story is not complete. There is evidence that either our understanding of neutrinos or the details of the fission process inside the reactors is wrong. After a correction to parameters defining the expected antineutrino flux, a large number of reactor antineutrino measurements were found to fall short of expected values[3]. These deficits in flux are seen in a number of experiments spanning a wide range of distances from the neutrino source. One theory is that these deficits are evidence of a fourth neutrino type, the sterile neutrino, which does not interact via the weak force. This sterile neutrino would cleanly explain many anomalies seen but would fall completely outside the scope of the standard model.

Reactor physics using neutrinos to further our understanding of fission and the nature of matter is a unique intermingling of Nuclear and High Energy physics. The opportunity to further develop both of these fields with relatively simple studies, such as the future PROSPECT experiment, is an exciting opportunity for future research to follow.

1.1 Reactors

Oak Ridge National Laboratory (ORNL) (the future site of the PROSPECT experiment) has a long history in reactor physics. Its first reactor, the Graphite reactor, was developed in the 1940's as part of the Manhattan project to generate Plutonium from Uranium slugs[4]. This reactor shown in Figure 1.1 went on to be the first reactor used to produce electricity from nuclear energy, examine radioactivity health hazards, and study the nature of matter. Since then, many scientists have studied fission and reactor physics to better understand nuclear reactions and how to control the immense power behind nuclear energy.

It is unsurprising that ORNL is still a world leader in reactor physics. The High Flux Isotope Reactor (HFIR) at Oak Ridge is one of the few remaining Highly Enriched Uranium reactors today. Built in the 1960's, HFIR is one of the largest producers of Californium in the world, vital for research across many fields[5]. The neutron studies conducted at HFIR have many applications in both bio-sciences and materials studies.

It is more than suitable that a neutrino physics experiment were to return to these historical grounds, with the aim to not only further our understanding of the fundamental laws governing the universe, but to also improved our understanding of reactor operations.

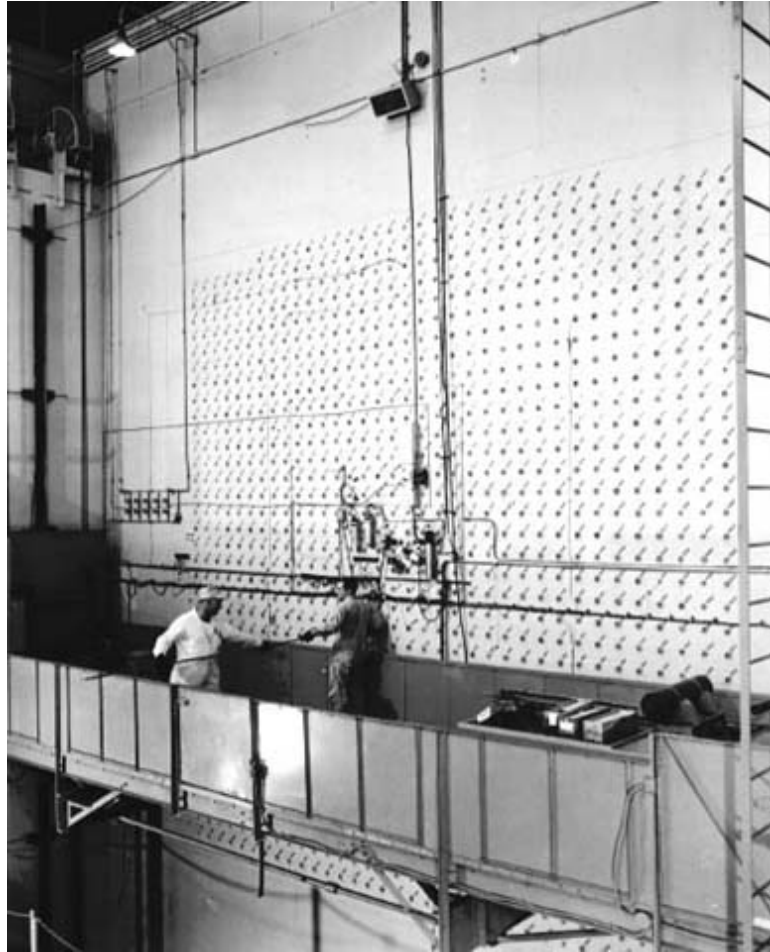


FIGURE 1.1: Graphite reactor at Clinton laboratories, now referred to Oak Ridge National Laboratory.



FIGURE 1.2: Image of reactor pool inside HFIR.

Chapter 2

Motivation

Neutrinos hold the key to understanding the secrets of complex systems that are otherwise untouchable. One example is the Sun: solar neutrinos from the core make it to the sun's surface within seconds after production. Information carried out by photons produced in the core however can take thousands of years to reach the surface, introducing uncertainties in the reactions they represent. Having reliable measurements of neutrinos produced in the sun creates a clearer picture of the reactions occurring in the Sun's core.

Reactors have played a key role in neutrino physics since their discovery in 1956. This is largely due to the reliability of the reactor operations combined with the sheer number of neutrinos a reactor can produce. Considering the reliability and experience scientists have with reactors, there are still a number of unknown properties of the neutrino. Reactor antineutrino anomalies have become a priority to both High Energy and Nuclear physicists as better understanding their properties probes questions in both fields. Does the lack of observed antineutrinos at reactor sites represent a misunderstanding in nuclear physics, preventing us to fully utilise the energy available in nuclear reactions? Or are these anomalies evidence of a fundamental misunderstanding in the standard model, providing evidence of the existence of a new particle?

2.1 Fission

Fission of a nucleus physically means the nucleus splits into two smaller isotopes. This radioactive decay can occur whenever the process will release energy and therefore is energetically favorable. In practice, this process only naturally occurs in the heaviest elements where the binding energy is quite low, making the nucleus unstable. Near stable

heavy elements are all neutron rich, hence the resulting fissile fragments are also neutron rich and often are far from stability. After fission, these products will then also undergo radioactive decay, either by β -decay or by β -delayed neutron decay towards stability. During the fission process, energy is released by a combination of kinetic energy in the direct fission products, and radiation released during subsequent decays. These decays include fissile fragments, γ -rays, neutrons, e and $\bar{\nu}_e$. Due to their electric charge, the fissile fragments and e have very short ranges and lose all their kinetic energy within the reactor. Although some γ -rays and neutrons deposit their energy within reactor core, a large number escape, contributing to the background radiation immediately around the reactor core. Only the $\bar{\nu}_e$ escape with their complete flux due to their low interaction cross-section[6].

In the heart of the reactor, fission of heavy elements is the main source of energy. In modern reactors, the four main fissile isotopes are ^{235}U , ^{238}U , ^{239}Pu and ^{241}Pu . Each of these fissile isotopes has certain advantages and disadvantages for both research and power production. Since HFIR uses ^{235}U as its fuel source, this work will concentrate on this on fission induced from this isotope.

On its own, ^{235}U is stable to fission. However, in the presence of neutrons ^{235}U can capture one, creating unstable ^{236}U . The ^{236}U will then fission into two lighter mass isotopes (discussed in more detail below) and often release a number of neutrons. The neutrons released during this process can then proceed to interact with other ^{235}U atoms within the reactor core, resulting in a self driven chain of reactions. The rate of reactions can be controlled by controlling the number of thermal neutrons within the reactor. Control rods which absorb thermal neutrons can be inserted in the ^{235}U fuel, preventing more fuel from becoming unstable. The control rods themselves are made from materials with high neutron capture cross-sections, such as Boron and Cadmium[7].

2.1.1 Fission Yields and Energy

The fissile products of a ^{235}U decay cannot be uniquely determined until after the process happens. The fissile products do however follow a statistical pattern. Presented here as Figure 2.1, one can see the statistical process forms two peaks, where each fission event is likely to produce an isotope from each peak. Additionally, many of the fissile products will be in unbound states after the initial division, meaning they will release a number of neutrons as well.

As an example of the fission process we will examine one possible fission event:

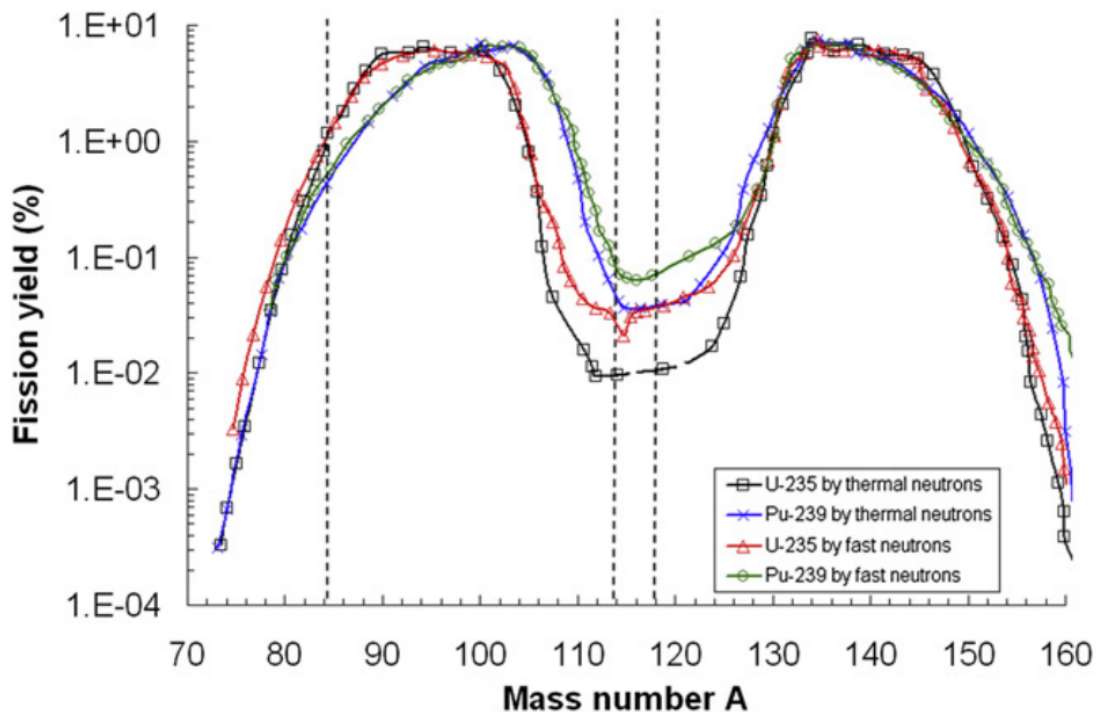
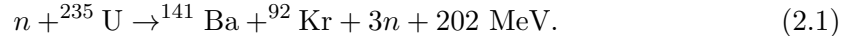


FIGURE 2.1: Fission yields of various fuel sources, adapted from Ref. [8].



A total energy of 202 MeV is released in this reaction of eq. 2.1, this energy comes from the mass difference between the initial and final products. Of this released energy, ~ 170 MeV is split as kinetic energy between the two fissile fragments. Five and 7 MeV go into prompt neutron and gamma emission respectively[6]. The remaining energy is disseminated through the fissile products' decay radiation. ~ 6.5 MeV is transferred into β^- particles, ~ 6.5 MeV is transferred into γ -ray emission and the remaining ~ 7 MeV going into the $\bar{\nu}_e$.

2.1.2 Decay Paths

Once the fissile products come to rest, they begin their decay back to stability. An example of this decay path is presented here in Figure 2.2. It is during this process that the antineutrinos of interest to the present work are produced. The decay described in 2.1 undergoes 7 total decays, hence producing 7 $\bar{\nu}_e$ in total. On average, a single fission atom of ${}^{235}\text{U}$ plus a neutron produces ~ 6 neutrinos[6].

During operation, the HFIR reactor produces 85 MW of energy. With the known conversion of $1 \text{ eV} = 1.602 \times 10^{-19}$ joules, and understanding how the fissile products decay

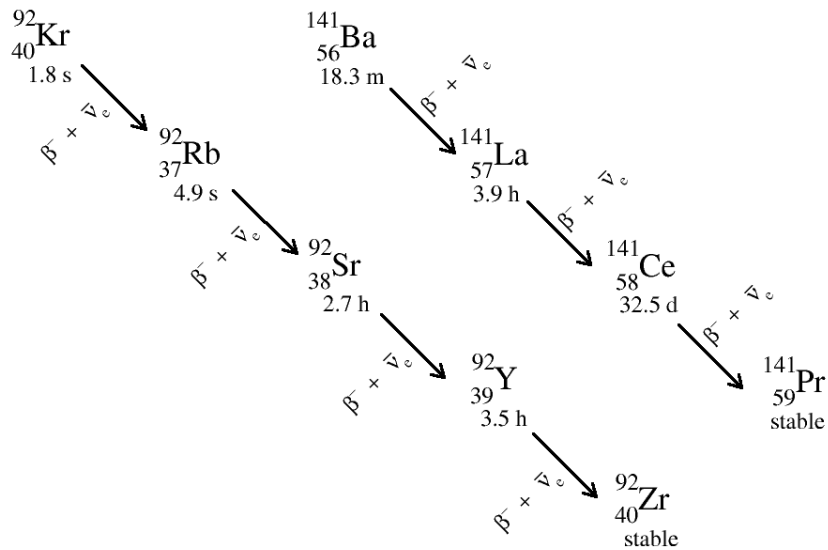


FIGURE 2.2: Decay paths back to stability following the fission of $^{235}\text{U} + n$ into fissile products ^{141}Ba and ^{92}Kr .

back to stability we can estimate that $\sim 8 \times 10^{18}$ $\bar{\nu}_e$ are produced every second in the reactor. While this is a sizeable number, one should remember that antineutrinos interact very poorly with matter. Additionally, with 10 times as many γ -rays being released at the same time, detection at the very close distances of the future PROSPECT detector to the reactor are a formidable challenge.

2.2 Reactor Neutrinos

As described above, reactors are very intense sources of neutrinos. Because of this, they have a long history of being used in neutrino studies from their initial discovery to the most recent neutrino oscillation studies.[3].

2.2.1 Neutrino Detection

The dominant method of reactor neutrino detection is the so called inverse beta decay (IBD) process. This method has proven to be remarkably efficient at extracting an antineutrino signal interacting weakly from the background. The process is described below:

$$\bar{\nu}_e + p \rightarrow e^+ + n, \quad (2.2)$$

The $\bar{\nu}_e$ interacts with a proton, resulting in a positron and a neutron being emitted. The positron quickly annihilates with an electron in the medium, producing two 511 keV γ rays. The neutron is also captured in the detector, releasing its own specific signature. The unique coincidence measurement between the two 511 keV annihilation photons and the captured neutron has proven to be an invaluable tool, isolating antineutrino interactions in a number of world class reactor based experiments.

A recent experiment to use IBD to detect antineutrinos is the Daya-Bay experiment, based at a large power reactor in southern China[9]. The detectors for this experiment are large pools of scintillating liquid, surrounded by photo-multiplier tubes to collect the light produced from the IBD signature. Daya-Bay has successfully collected measurements of the reactor's antineutrino flux and energy spectrum. Figure 2.3 plots the Daya-Bay measured antineutrino flux relative to other reactor neutrino measurements.

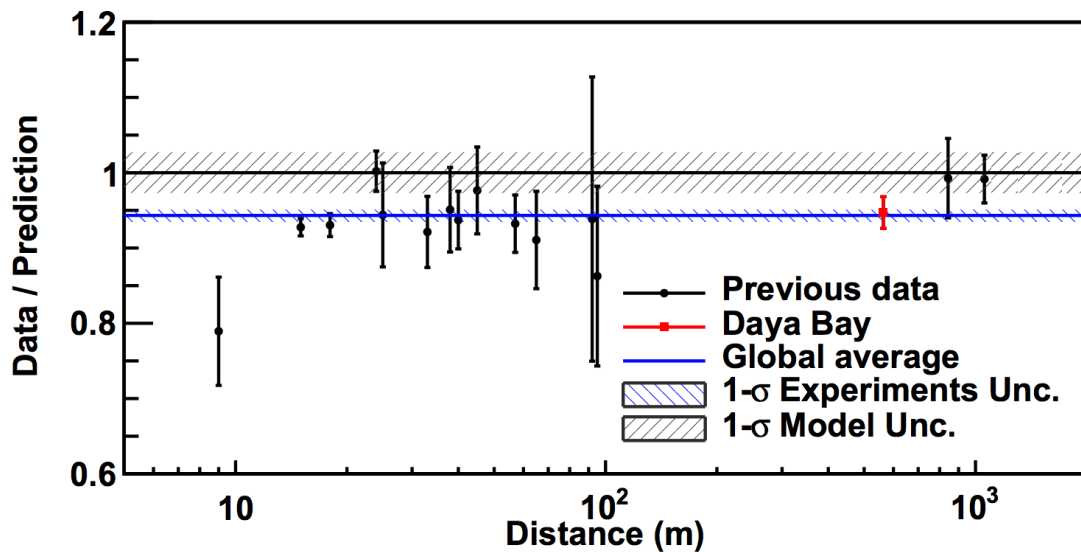


FIGURE 2.3: Antineutrino flux measured by different reactor experiments, highlighting Daya-Bay's measurement[9].

The future PROSPECT detector will also utilize the IBD process for neutrino detection. The PROSPECT detector (described below) contains a ${}^6\text{Li}$ -doped liquid scintillator. This scintillator has a relatively high efficiency for detecting antineutrinos from the large neutron cross-section of the ${}^6\text{Li}$. Further, the high light output from the scintillator makes it ideal for background discrimination. Figure 2.4 is a visual diagram of how the IBD signal is formed in the ${}^6\text{Li}$ doped scintillator.

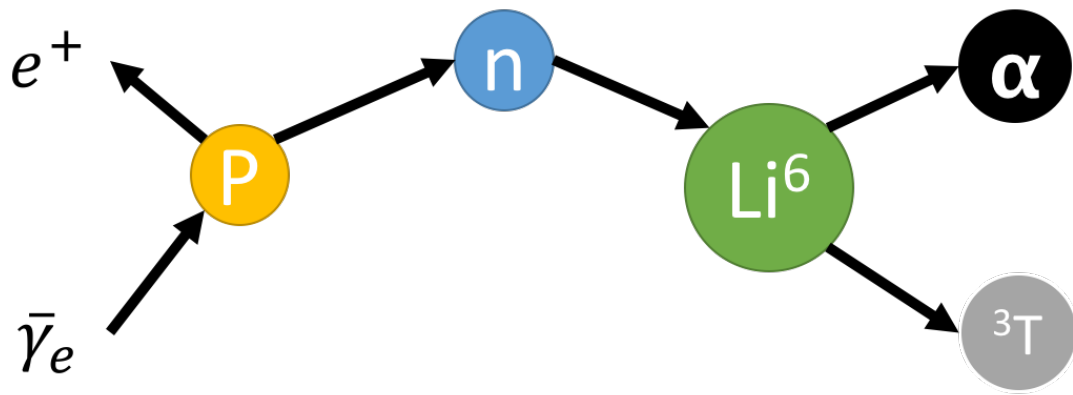


FIGURE 2.4: Diagram of the IBD process occurring in a ${}^6\text{Li}$ -doped scintillator interaction with antineutrino.

2.2.2 Reactor Antineutrino Anomalies

While neutrino measurements in reactors have shed light on many of the neutrinos properties, the same measurements have also provoked their own questions. Disparities have been seen in measurements of the neutrino flux using the IBD method and predicted antineutrino flux from various model calculations.

As seen in figure 2.3, a large number of reactor antineutrino flux measurements have seen a deficit from predicted antineutrino flux. On average, there is a 5-6% deficit in measured flux from predicted values. This deficit is referred to as the reactor anomaly. There are a number of theories as to how this deficit formed. One possibility for the anomaly is inaccurate or incomplete data used to make the predicted models in the neutrino flux. Another possibility for the deficit is a miscalculation of the reactor emissions. The decay chains and expected antineutrino fluxes may not be well enough understood, so the predicted flux is too large. The lack of inclusion of beta delayed neutron decay in the antineutrino flux calculations could be the reason for the miscalculations[10].

Another possibility is the existence of a fourth flavor of neutrino which would fall completely outside the standard model. Such a neutrino would not interact with the weak force, and hence is commonly referred to as a sterile neutrino. As a sterile neutrino would only interact with matter through gravity, if it was present it would appear as a deficit in the measured flux. If the other types of neutrinos could oscillate into the sterile neutrino flavour, then the predicted fluxes would be greater than the actual value.

The discrepancy in measurements to predicted values continues in reactor antineutrino measurements with an increase of 4-6 MeV antineutrinos from the predicted flux[11]. This is colloquially referred to as the 'bump'. The bump has been seen in a number of

antineutrino reactor measurements, including Daya-Bay. Figure 2.5 is a display of the Daya-Bay antineutrino spectrum flux where this bump can be seen.

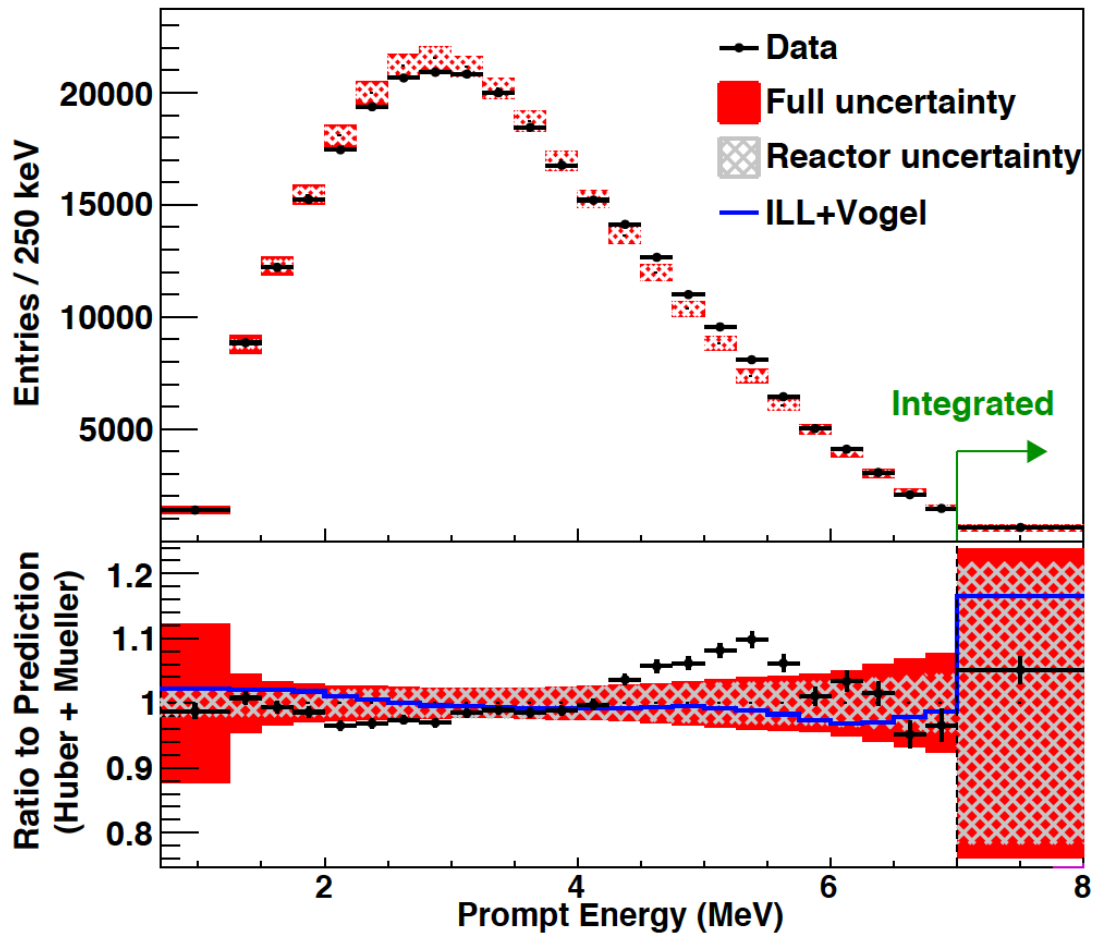


FIGURE 2.5: Daya-Bay antineutrino spectrum illustrating bump in the 4-6 MeV region[9].

As described in Ref. [11], the source of this bump is still not clear. However, an isolated antineutrino spectrum from only a single fissile isotope should help shed some light on potential sources. PROSPECT plans to generate this very spectrum from an isolated ^{235}U source at HFIR, with high precision and over very short baselines. Hopefully this method of measurement will answer questions about both the deficit and the bump.

2.3 PROSPECT Experiment

The Precision Reactor Oscillation and Spectrum Experiment, (PROSPECT), is a short baseline neutrino experiment to be located at ORNLs HFIR. The collaboration is made up of approximately 65 scientists, involving universities and laboratories across the United States. PROSPECT has three main physics goals:

- Define the worlds most precise antineutrino energy spectrum
- Resolve anomalous results in antineutrino flux
- Provide evidence for or against the existence of sterile neutrinos

PROSPECT's experimental setup schematic is presented here in Figure 2.6.

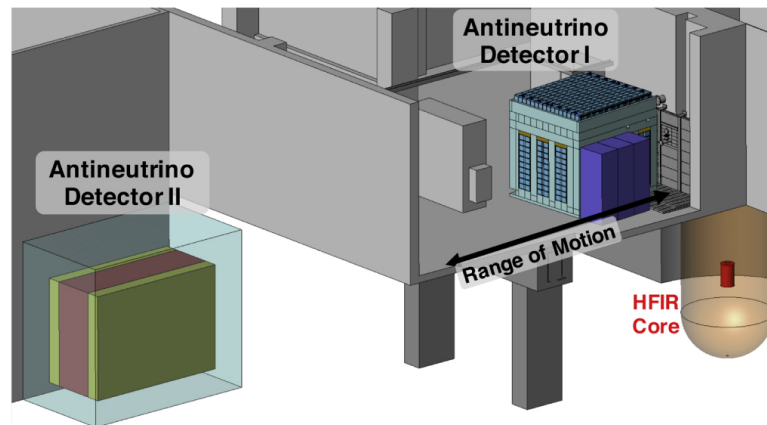


FIGURE 2.6: Diagram of PROSPECT detector location relative to HFIR core[12].

PROSPECT will ultimately be composed of 154 optical separated segments[12]. Each detector segmented is consists of a ${}^6\text{Li}$ -doped liquid scintillator cell with two PMT read-outs. The liquid scintillator detects the antineutrinos by measuring inverse beta decay as previously discussed. The signature of this radiation is measured and used to identify the antineutrino's energy and position within the scintillator cell.

The PROSPECT detector will be mobile, measuring antineutrinos in three positions from 7 to 12 m from the reactor core. These unique features should allow PROSPECT to measure the most precise antineutrino energy spectrum and antineutrino flux at these very close ranges. It is believed these precise measurements will clarify anomalous results regarding the antineutrino flux measured at a number of other experiments, providing definitive evidence on either the existence or non-existence of a sterile neutrino.

2.3.1 PROSPECT at HFIR

Measurements for PROSPECT will be carried out at the High Flux Isotope Reactor (HFIR). HFIR is a highly enriched ${}^{235}\text{U}$ (Uranium-235) reactor (HEU) with not only one of the highest neutrons fluxes in the USA but also one of the highest average power densities[5]. As previously discussed, reactors provide a large sample of antineutrinos above the minimum energy of 1.8 MeV to be measured using the IBD process for PROSPECT to measure.

The reactor itself enriched to 93% ^{235}U and 7% ^{238}U . For comparison, industrial nuclear reactors usually contain less than 20% ^{235}U and more than 80% ^{238}U . The highly enriched core means that throughout the cycle the radiation given off is nearly entirely from the neutron induced fission of ^{235}U , allowing for more accurate model predictions to be made of the fissile products and their daughters. The cleanliness of the fissile products ultimately reduces the uncertainty in the predicted antineutrino spectrum making the comparison to the future measured spectrum more accurate.

The detector's location is unique as there is an easily accessible space for a 4-ton detector very close to the reactor's core in the experimental hall. Traditional short base line reactor neutrino experiments are positioned nearly 100 meter from the reactor cores. PROSPECT's very short distance will increase neutrino flux and allow the experiment to probe the distances predicted to be the most sensitive to sterile neutrino oscillations but it comes at a cost. This area is exposed to large fluxes of background radiation from numerous sources, beam lines, and the reactor itself. PROSPECT requires a detailed spatial and temporal study with the exact locations and time variation of the radiation even though the total background radiation in the area is well below safety thresholds[5].

HFIR runs in cycles for approximately 24 days before the fuel is spent and the reactor is shut off. The time between cycles can vary from 18 days to 3 months depending on the desired and necessary maintenance. These cycles are a key tool for PROSPECT's background subtraction[12]. PROSPECT plans to use radiation measured during a reactor off period to further understand the cosmogenic and room background sources. This measured background will ultimately be key to fitting the antineutrino spectrum.

Figure 2.7 is a diagram of where the PROSPECT detector will be located in its two most extreme positions at HFIR (7m and 12m from the core). The PROSPECT detector will sit above two neutron beam lines, HB-3 and HB-4. These neutron beam lines on the floor below can be seen in Figure 2.7.

HFIR has a number of experimental beam lines which transport radiation from the core to other areas at the facility. This complicates the radiation profile in the room as it distributes the sources of the radiation to multiple locations. HB-3 is one such neutron beam line that splits off to two neutron diffractometers[13]. Another beam line, HB-4, is designed to transport cold neutron and leads to a number of neutron diffraction experiments being conducted in an experiment hall 10m away[5]. The PROSPECT detector measurements will take place in two different rooms: the experiment room and the MIF experiment room. The location of these two rooms is also highlighted in Figure 2.7 with respect to the reactor core and beam lines.

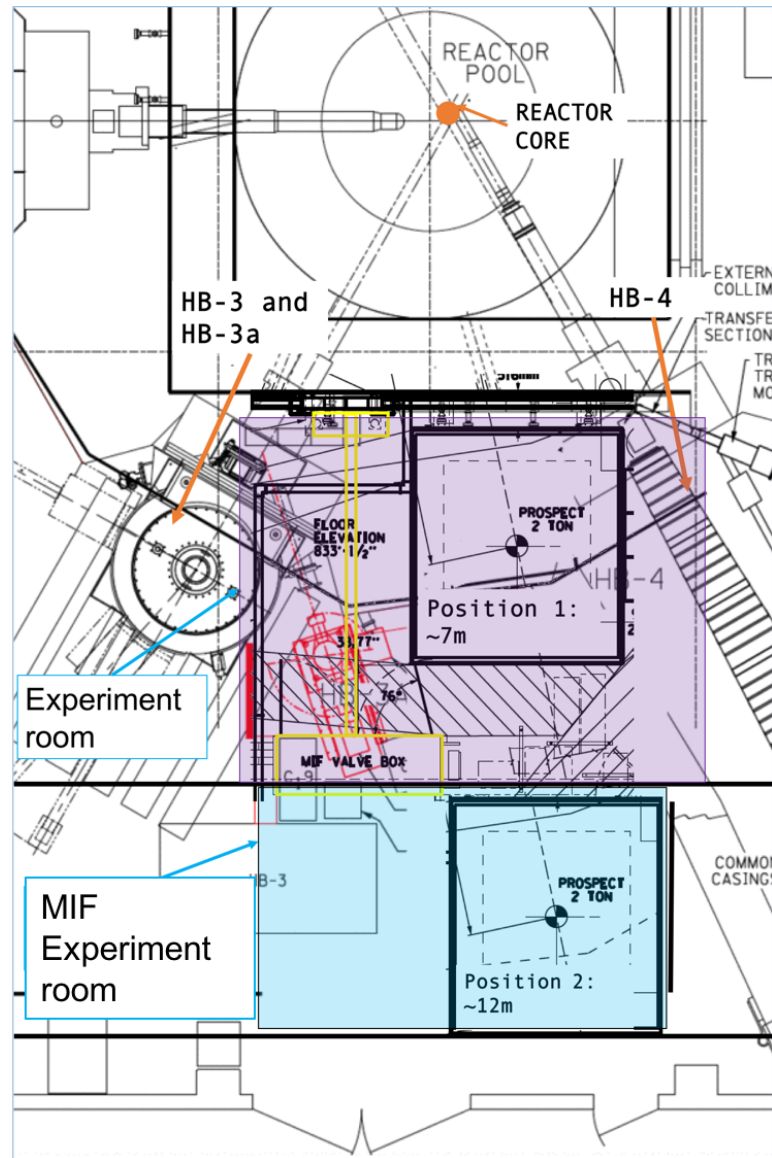


FIGURE 2.7: Diagram of PROSPECT detector locations and neutron beam lines at HFIR.

Chapter 3

Radiation Detection

Even though radiation surrounds us in our day-to-day lives, accurate detection and classification requires careful examination. The PROSPECT detector will be located only a few meters from the HFIR core. At the heart of the reactor, the fission process produces a large number of both neutrons and γ -rays as a by-product. Even with shielding surround the reactor core, PROSPECT will still be exposed to immense γ -ray and neutron radiation fields while looking for small fluctuations in the observed antineutrino spectrum.

To observe antineutrino spectrum fluctuations in the presence of such intense fields requires the support of a detailed background characterization. Both γ -rays and neutrons (like the desired neutrinos) are chargeless and have a high penetrating power, therefore are very likely to make it from the reactor to our detector setup.

The primary aim of this project is characterizing and understanding the large background fields produced in close proximity to the reactor. Characterisation was done by measuring γ -ray and neutrons fields produced while the reactor was on and comparing them to fields observed when the reactor is off. However, the way that γ -rays and neutrons interact with matter is different. Each requires dedicated detectors, with some better at extracting certain properties of the radiation such as time, energy, or absolute flux. Therefore many types of detectors are used to provide a more robust measurement of the background radiation.

In order to detect a quantum of radiation, ultimately the particle must interact with a detecting element and deposit some or all of its energy. This interaction produces a charge pulse which can in-turn be analyzed. Detectors are near universal in that they use the incoming radiation to ionize atoms within the detecting volume to spot the

radiation. The variations in detecting material and design can be optimized so that the maximum information with the smallest error can be extracted.

3.1 Gamma-ray Interactions

The reactor core produces γ -rays with energies spanning ~ 100 keV to 10s of MeV. In this energy range, γ -rays interact with matter in three basic processes; photo-absorption, Compton scattering, and pair production[14]. Each of these three interactions has a different probability of occurring, depending on the energy of the incident γ -ray and the Z of the detecting material.

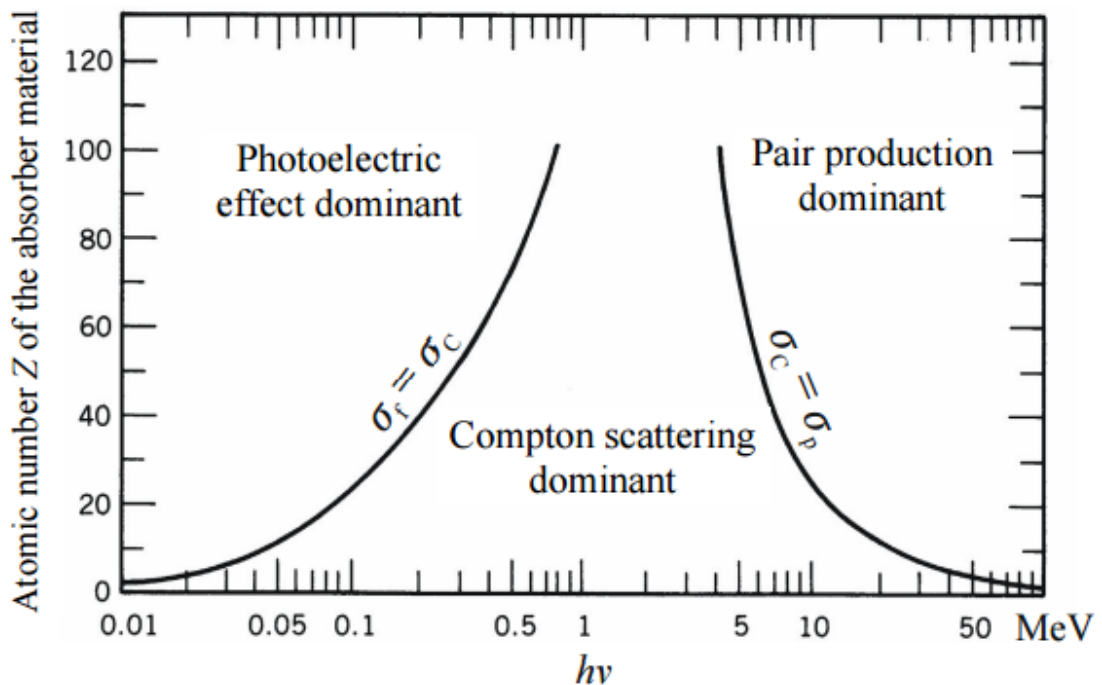


FIGURE 3.1: Figure describing the different interactions of γ rays with matter[15].

As seen in Figure 3.1, the low energy γ -rays interact mostly by photo-absorption. Photo-absorption involves a photon imparting all of its energy on an orbital electron. The electron is ejected from the atom but then quickly stopped after interacting with other electrons in the material. The electron released in this process will have a kinetic energy proportional to the energy of the incident photon, allowing the interaction to be accurately be converted to an energy signal[14].

As the photon energy increases, the probability the γ -ray will undergo photo-absorption decreases and the probability it will Compton scatter increases. Compton scattering is the colloquial term for a γ -ray inelastically scattering off of a valence electron. This process results in the incoming γ -ray imparting some of its energy to the scattered

electron with the rest of its initial energy being released as a lower energy γ -ray[14]. The sum of the scattered electron's energy plus the "scattered" photon's energy will equal the initial photon's energy. A diagram of the Compton scattering interaction is presented here as Figure 3.2.

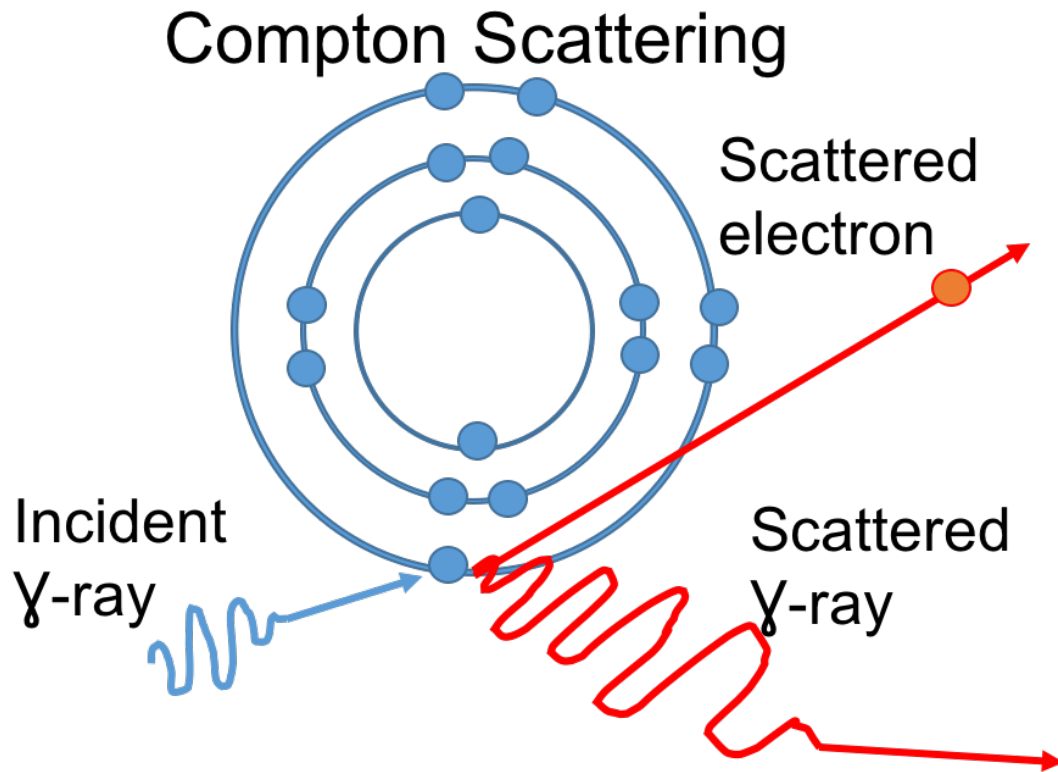


FIGURE 3.2: Image of incoming γ -ray interacting with orbital electron, imparting some of its energy onto the electron and the rest continuing as a lower energy γ -ray.

Depending on the scattered photon's energy, it could Compton scatter again onto another atom in the detecting material or simply undergo photo-absorption. This process will continue until either the "scattered" photon is photo-absorbed or escapes the detecting material. If the entire incoming γ -ray is absorbed, the sum of all the scattered electrons will be proportional to the energy of the incident γ -ray, contributing to a full energy peak. However, if at anytime the "scattered" γ -ray escapes the material, the produced signal will have some value less than the proportional value to the energy of the incident radiation. These escaped events are commonly referred to as the Compton background[16].

The third primary γ -ray interaction with matter is pair production. In the presence of an atom, a γ -ray with at least twice the rest mass energy of an electron (511 keV) is energetically allowed to transform into an electron-positron pair[16]. The probability of pair production increases with both the energy of the incident γ -ray and the Z of the material it is present in[16]. In this process, the sum of the electron and positron's rest

mass plus the imparted kinetic energy to the pair will be equal to the energy of the incident γ -ray. Both the electron and positron will quickly come to rest in the detecting material. Once the positron comes to rest, it will annihilate with an atomic electron, releasing two characteristic 511 keV γ -rays. Either one or both of these two γ -rays will Compton scatter or be photo-absorbed, therefore be detected. Pair production results in a smaller peak in the energy spectrum to be seen 511 keV or 1022 keV less than the full energy peak. These peaks are colloquially referred to as the first and second escape peaks, respectively.

3.2 Scintillation Detectors

Detecting radiation with scintillating materials is one of the first known methods of converting radiation into an electronic signal. A scintillator is a material that emits light when impinged by ionizing radiation. This process happens due to the particle essentially knocking electrons out of the valence band of the crystalline structure into a conducting band. As the electrons fall back into the valence band, there is a release of photons in the visible to near-visible range.

One problem which arises from such a process, is the emitted photons from the scintillator can be reabsorbed by the scintillating material, where the emitted photons cannot penetrate the scintillator itself. To combat this effect, impurities are often added to the scintillating material, called activators. The activators must be chosen carefully so they only result in discrete states within the band gap and are not populated directly. As the electrons decay back to the valence band, they pass through the activator states slightly changing the wavelength of photons emitted by the scintillator, allowing the light to more easily pass through the scintillating material.

This altered wavelength from the scintillating material is matched with a proper photo multiplier tube (PMT) to convert the photons into an electronic signal. As the number of initial knocked out electrons is directly proportional to the energy of the incoming particle, the produced electronic signal is also proportional to the energy. The width of the peak produced from radiation of certain energies is one metric on how well the scintillator performs. This width is governed by the Poisson distribution[14]:

$$P(x) = \frac{(pn)^x e^{-pn}}{x!} \quad (3.1)$$

where p is the number of total possibilities and n is the number of measurements made. From equation 3.1, it follows that the variance of the distribution is:

$$\sigma = \sqrt{\langle x \rangle}. \quad (3.2)$$

were x is the number of charge carriers, or photons produced through the scintillation process. The figure of merit for the resolution in γ -ray spectroscopy is therefore the full width of the peak at half of the peak's maximum value (FWHM). The FWHM is related to σ by:

$$\text{FWHM} = 2\sqrt{2\ln(2)}\sigma. \quad (3.3)$$

3.2.1 Sodium Iodide NaI(Tl) detector

Sodium Iodide scintillating detectors are the most widely used scintillators in γ -ray spectroscopy[16]. While this is largely due to historic reasons, they continue to maintain their popularity with their large efficiency, reasonable energy resolution, radiation hardness, and easiness of producing large crystals[14]. While the absolute efficiency of γ -ray detection is critical, a larger volume NaI(Tl) detector can provide a substantial efficiency and limit the number of electronic channels.

3.2.2 Cerium Bromide CeBr₃) detector

A relatively new detecting material, CeBr₃ is an attractive alternative to NaI(Tl). The intrinsic properties, both energy and efficiency, of CeBr₃ make it ideal as a γ -ray detector. Being a scintillator, the detection method is similar to NaI(Tl). The energy resolution, however, is much better, as highlighted here in Table 3.1. CeBr₃ is directly comparable to another scintillator detector listed in Table 3.1, LaBr₃. Figure 3.3, shows the spectrum for a NaI(Tl), CeBr₃ and LaBr₃ scintillator detectors for comparison.

There are other γ -ray detectors with better energy resolution than CeBr₃, however they come with their own trade-offs and complications. One is the LaBr₃ detector[17], as mentioned briefly above. These crystals come with their own intrinsic radioactivity impurities in the La which α -decays. This adds background counts, particularly in the 1500 keV and less region of the spectrum, decreasing the precision of the measurements taken of lower energy peaks. Semiconductors also offer a far better energy resolution[16]. The gold standard in γ -ray spectroscopy is the Highly Purified Germanium (HPGe) detector which achieves resolutions of 0.2% at 1 MeV. Unfortunately HPGe detectors have a low efficiency, need to be kept at cryogenic temperatures, and can be sensitive to microphonics, making them inconvenient for use on a mobile array like DANG[16].

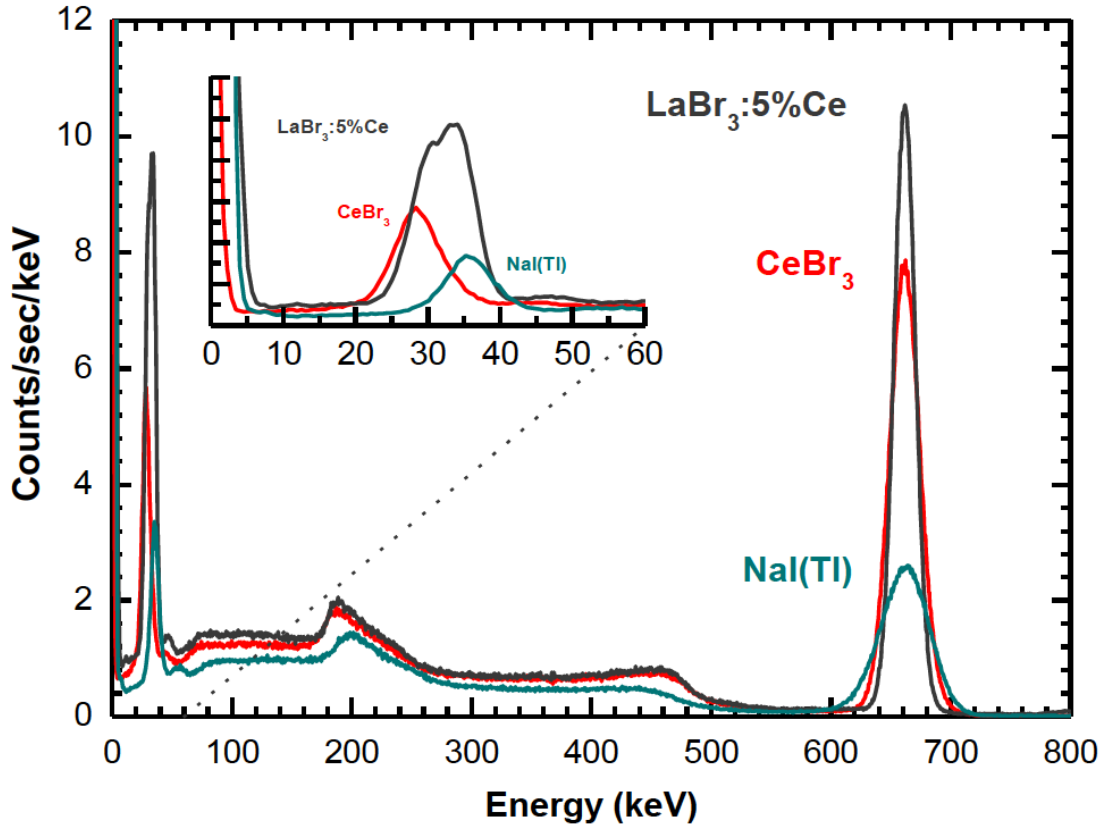


FIGURE 3.3: Spectrum taken from a CeBr_3 , a $\text{NaI}^{(Tl)}$ and a LaBr_3 detector with a ^{137}Cs source. Figure is adapted from ref. [17].

TABLE 3.1: Light output and percent resolution for various scintillators discussed in the text. All numbers are approximate and should only be used for discussion. Photomultiplier efficiency is assumed at 15% in the tabl.

	Photons per MeV	Photons Collected	σ (FWHM)	Percent Resolution
$\text{NaI}^{(Tl)}$	38000	5700	75 (180)	3.2 %
LaBr_3	63000	9500	97 (230)	2.4 %
CrBr_3	59000	8900	94 (220)	2.5 %

Microphonics are where electronic systems turn mechanical vibrations into electronic signals, introducing noise into the system.

3.3 Neutron Interactions

Similar to γ -rays, neutrons have no electrical charge and can travel several centimeters before interacting[16]. Neutrons interact with matter differently depending on the

material and the neutron energy, therefore the detectors used to detect them are quite diverse. This research project will discuss two main methods of interaction: the $(^3\text{He},n)$ interaction and elastic scattering.

Elastic scattering is the collision of two particles where the kinetic energy is conserved in the frame of the center of mass. Neutron elastic scattering occurs more regularly with atoms of a similar size to the neutron, like Hydrogen, so the kinetic energy is split more evenly between the two particles[16]. In a hydrogen rich detecting material, neutrons can easily scatter many times, with each collision producing a recoil proton. Recoil protons in turn interact with atomic electrons in the material and quickly come to rest. Again, due to energy conservation, the sum of the kinetic energy of all the recoiled protons equals the kinetic energy of the incoming neutron. This kind of detection is ideal for a neutron with a kinetic energy over $\sim 100\text{keV}$, referred to as fast neutrons.

Slow neutrons (neutrons with energy $<100\text{ keV}$) have a small kinetic energy therefore deposit very little energy when they elastically scatter, making them hard to detect with through elastic scattering. However, their low kinetic energy results in them slowing down to thermal equilibrium with the medium which we can use to identify the particle. An example of this kind of interaction is $(^3\text{He},n)$. $(^3\text{He},n)$ has a high cross section with slow neutrons, but they are insensitive to the energy of the incoming neutron. This is due to the release of energy in the $(^3\text{He},n)$ reaction 3.5.

3.3.1 Fast Neutron Detectors, NE213 Liquid Scintillator

NE213 is a liquid scintillator for fast neutron detection and spectroscopy. It was produced by Nuclear Instruments and is currently referred to as EJ-301[16]. The liquid has a large ratio of hydrogen to carbon atoms, increasing the probability of a neutron interacting with a hydrogen atom[18]. As mentioned before, the fast neutron has a high cross section with the hydrogen in the the hydrocarbon chain. The hydrogen is knocked off the hydrocarbon chain when the fast neutron collides with it, releasing a recoiling proton. The recoiling proton interacts in an electronic field with the rest of the detector's active volume, creating light. Equally, when a photon or γ -ray enters the liquid, it Compton scatters off of the hydrogen atoms in the scintillator's hydrocarbon chains. This Compton scattering also creates light in the liquid scintillator, however it creates a very different shaped electronic pulse compared to the neutron scattering. A figure of merit is used to measure the shape of the electronic pulses and distinguish between the two interactions. The figure of merit is called pulse shape discrimination or PSD[16] and is defined by Equation 3.4:

$$PSD = \frac{Q_L - Q_S}{Q_L} \quad (3.4)$$

Q_L is the integration of charge over a large portion of the electronic pulse, or long gate emitted from the detector. Q_S is the integration of charge over a short portion, or short gate from the electronic pulse. Figure 3.4 displays a typical description of how these gates are defined.

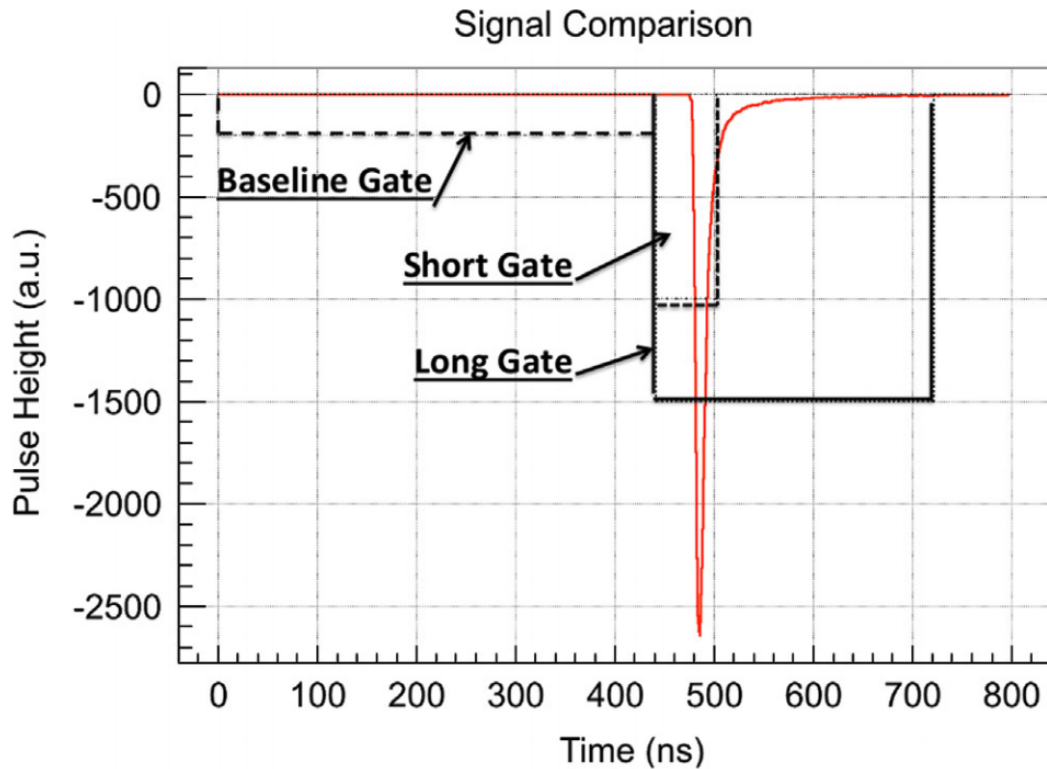


FIGURE 3.4: An image of an electronic pulse highlighting how the short gate and long gate are defined[19].

When the PSD is plotted against energy, two clear bands can be seen. One band contains the neutron induced pulses and the other contains the gamma induced pulses. The separation and therefore the resolution of these two bands can be increased by changing and optimising the length of integration for Q_L and Q_S , or the long and short gate.

Further discussion of optimising digital settings can be found in Section 3.4 or in Ref. [19].

3.3.2 Slow Neutron Detectors, ^3He Proportional Counter

In contrast to fast neutron counters, slow neutron detectors take advantage of nuclear reactions. Slow neutron detectors consider a large number of variables, but are primarily concerned with the cross-section and Q-value of the reaction[16]. A high cross-section is needed to maximize the neutron interaction in the volume while a large Q-value releases more energy, making the resultant charge particles easier to detect.

A common proportional detector which combines a high cross-section and a large Q-value is the ^3He tube detector. These detectors use the reaction 3.5 to detect neutrons:



The tube itself consists of high pressure gas with an anode centre and a cathode shell, applying a high voltage across the gas[20]. Figure 3.5 provides an illustration of how ^3He tubes are designed.

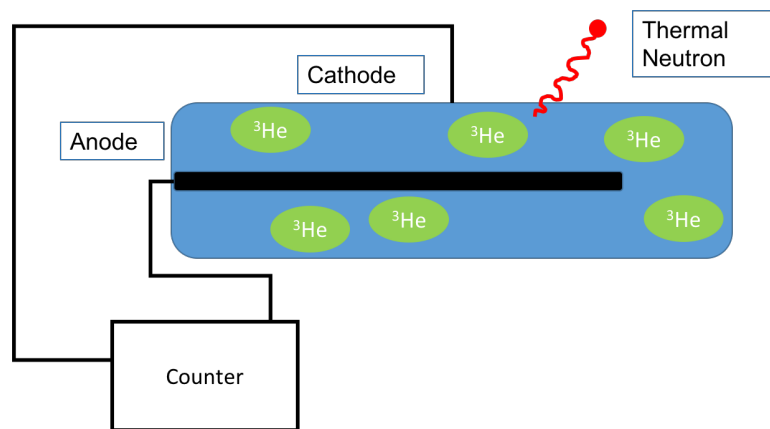


FIGURE 3.5: Diagram illustrating design of ^3He proportional counter.

DANG's ^3He detectors have a pressure of 10 atm and 2" in diameter by 24" long. An image of a pulse from the ^3He tube can be seen in Figure 4.14.

As highlighted in Equation 3.5, the ($^3\text{He},p$) interaction releases 765 keV of energy between the triton and proton, both of which are easily detected due to their charge. The cross-section for this reaction is large for neutrons at low energies and decreases as the neutron energy increases, as shown in Figure 3.6[21]. While this reaction allows for effective neutron measurement at low energies, every detection will produce 765 keV of energy. The result is all information about the initial energy or direction of the neutron is lost. However, this interaction has a very low cross section for γ ray interaction, increasing the accuracy in the flux measurements made, especially in large γ ray fields.

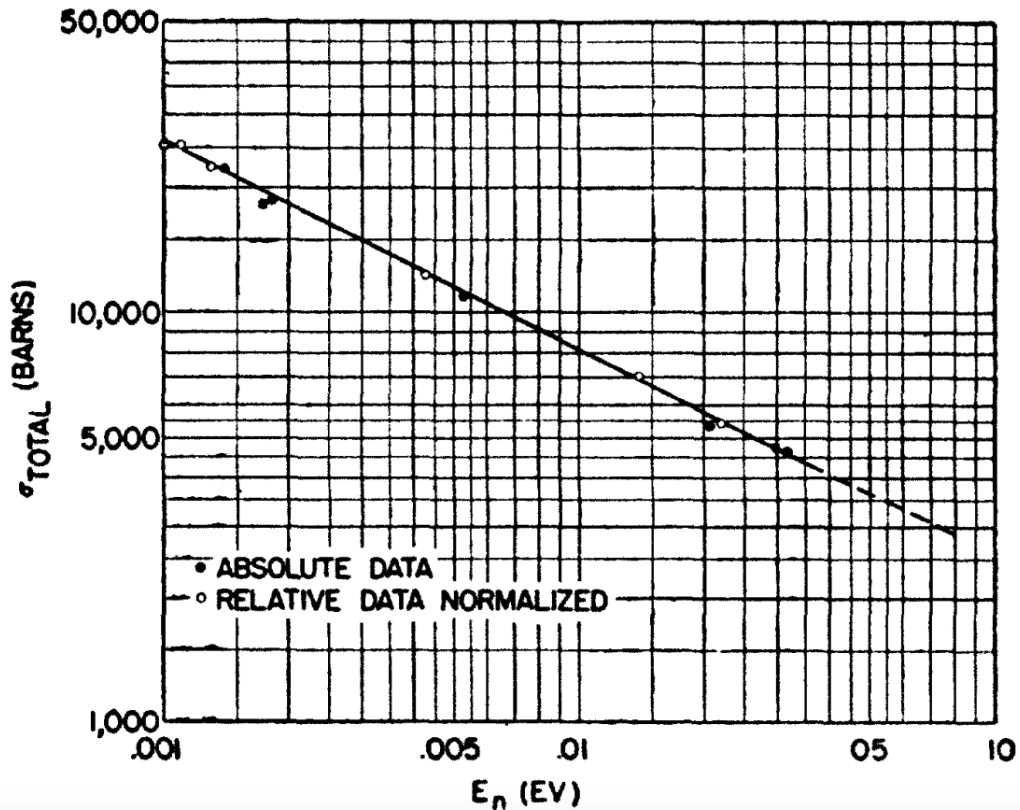


FIGURE 3.6: The total cross section of the ($^3\text{He},p$) interaction as a function of the incoming neutron's energy[21].

To further increase the efficiency of the ^3He tube detectors, they can be fit with polyethylene sleeves. These sleeves have a high proton content, which as described above is very efficient at slowing, or moderating neutrons. Once a fast neutron is slowed, there is a greater probability that it will undergo the ($^3\text{He},p$) reaction and therefore be counted by the ^3He proportional counter.

3.4 Pulse Shape Analysis

Once a detector converts radiation into a charge, the collected charge (or detector signal) needs to be converted into a digital signal, for example into the computer. Sometimes the detector signal is shaped, making it easier for the associated electronics to accurately convert the collected charge.

Nominally there are two major pieces of information which we desire to collect from each detector signal. The first is the amount of charge carried by the signal as normally this is directly proportional to the energy of the radiation impinged on the detector. The second is the time information of when the impinging radiation arrived at the detector.

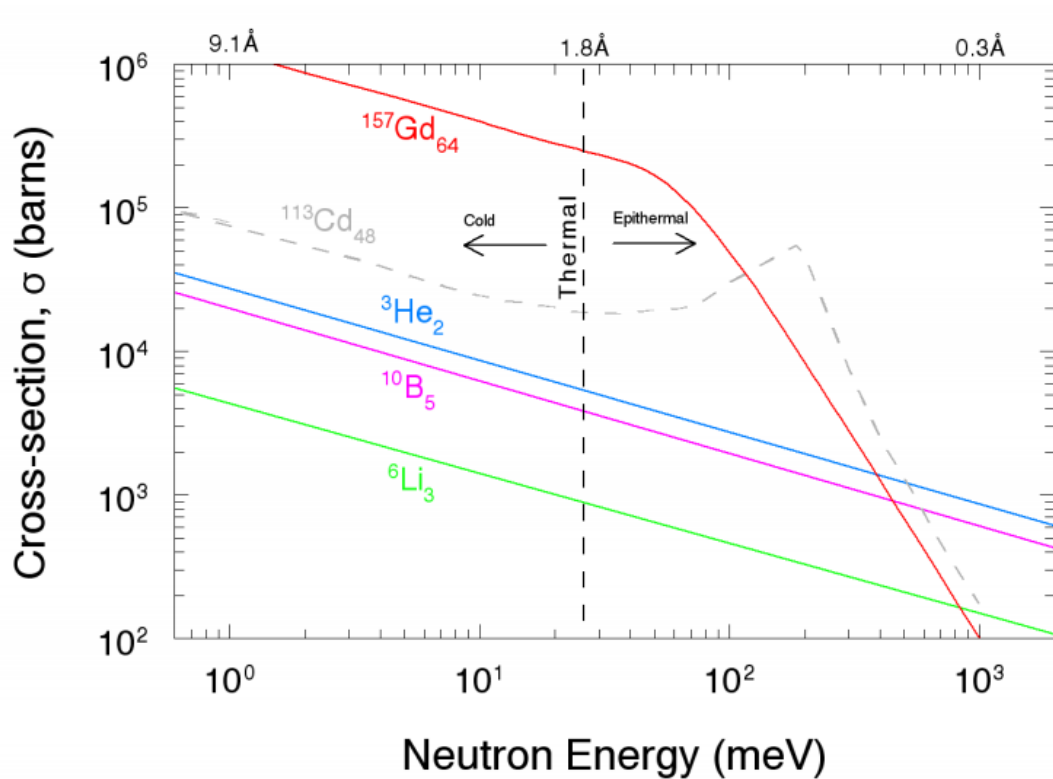


FIGURE 3.7: Neutron capture cross sections as function of neutron energy for various common gases used in proportional counters. Figure is adapted from ref. [22].

With these two pieces of information, one can construct and examine energy histograms and coincidence relations between different events and detectors.

For many years in physics, the signal shaping, converting, and digitization happened in series by a string of analogue electronics. In recent years however, flash digitizers have made it possible to convert the detector signal at the collection time. This has a number of advantages; one digital module can replace an entire chain of analogue modules, and improved timing and energy information can be extracted from the input signal. Only a modern digitizer was used in this project, therefore the discussion will be focused on that.

3.4.1 Digitizers

While the technical workings of a digitizer are quite complex, conceptually their operation is fairly straight forward. There are three main characteristics to any digitizer: its sampling rate, the number of bits in the flash ADC, and its maximum input voltage. Essentially, the digitizer samples a wire at the sampling rate (typical rates from 10s-100s of MHz) converting the amount of charge collected in each sample to a number between zero and its maximum input voltage[23]. The accuracy of this sample is described as

the number of bits the digitizer has. After this process, a digital copy of the waveform (as one would see on an oscilloscope) is stored in a computer.

Different algorithms can be run over this waveform to extract energy and timing information as well as pulse shape discrimination properties from the collected signal. Due largely to storage space and computer writing speeds, the waveform is rarely stored. Instead the algorithms extract the relative information run on the digitizer board itself and analyse the waveform live as the signal is collected.

3.4.2 Pulse Shape Discrimination

The way that the neutron and γ ray stop in the NE213 fast neutron detector is dissimilar. This variation results in different rise time behaviors for the energy deposited and collected in the detector. However once all the energy of the particle is deposited, the neutron and γ ray may have identical charge collected in the detector[16]. By setting short and long integration gates (sum regions) over the digitized pulse however, one can produce a ratio of the charge collection during the rise of the signal over the total charge of the signal[16]. This value should be constant yet distinct for both γ rays and neutrons, separating the two interactions. The PSD parameter is used in Figure 3.4.

Chapter 4

Detector Array to measure Neutron and Gamma-rays: DANG

As mentioned in the previous chapters, HFIR is the future home to the very short baseline neutrino experiment PROSPECT. Operating several feet from the reactor core, PROSPECT will be exposed to intense γ -ray and neutron fields produced from the fission inside the reactor and from other experiments running near the core which previous short baseline neutrino experiments did not have to deal with. While it is believed that the ${}^6\text{Li}$ doped detectors using the IBD process will be capable of extracting the true neutrino signal from the background radiation, this may still prove to be a formidable task. With this in mind, the current work was to quantify and map, in both space and time as a function of reactor cycle, fields produced within the experimental hall.

The Detector Array to measure Neutrons and Gamma rays (DANG) was built as a support system for the upcoming PROSPECT detector at HFIR. The primary goal of the array is to characterize the type, the location, the intensity, and the time evolution of background radiation throughout the future PROSPECT site. DANG is composed of a number of different types of detectors to provide a detailed description of the radiation fields. All of the detectors are mounted to a square aluminium structure, with a cross section approximately the same as the proposed PROSPECT detector. This allows the different detectors to sample a 'slice' of the volume PROSPECT will occupy in one measurement. Additionally, this aluminium structure with mounted detectors, associated electronics, and data acquisition system, is mounted to a mobile platform. This allows a large volume to be swept through with minimal setup time and limits systematic uncertainties.

Due to PROSPECT's close proximity to the reactor core (23 ft), one can expect rather large fluxes of both neutrons and γ -rays at a wide variety of energies. To help understand these fields, DANG is composed of different detectors, each being sensitive to either thermal neutrons, fast neutrons, or γ -rays. Furthermore, the electronic modules selected to operate DANG (both HV and digitizers) are either identical or very similar to the planned PROSPECT modules. This allows one to judge the performance of the modules at similar counting rates and in the same high radiation fields and similar electrical noise environments the future PROSPECT modules will see.

DANG's aluminium structure is 80 inches tall and the platform is 80" long by 47" deep. Figure 4.1 shows the size of DANG relative to the proposed PROSPECT detector size.

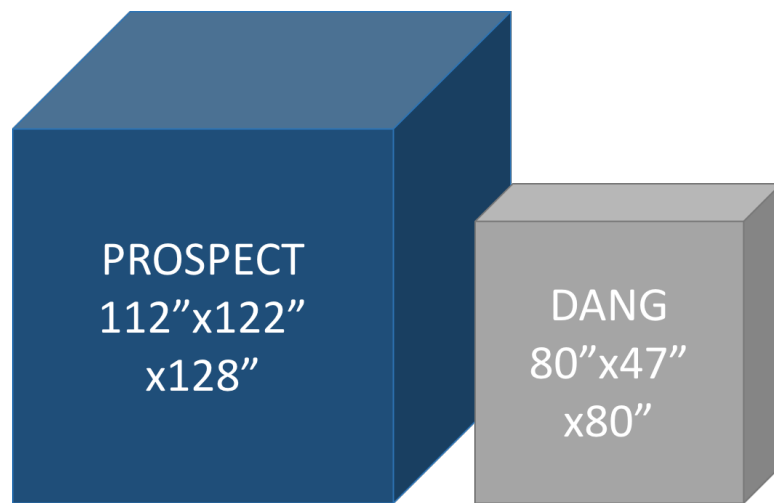


FIGURE 4.1: A comparison of the size of the detector array with the proposed dimensions of the PROSPECT detector.

The dimensions were selected such that DANG could efficiently sample the entire active volume of the future PROSPECT site while still fitting through standard doorways between rooms in HFIR. Fitting through doorways is a requirement for storage purposes and to conduct measurements in another room. Aluminum was chosen as the structural material because it is light, cheap, and does not have any long-lived activation products.

4.1 Detectors

The γ -ray fields are characterised by eight Sodium Iodide (NaI(Tl)) detectors and one Cerium Bromide (CeBr₃) detector. The CeBr₃ detector was only present for a small portion of the measurements. It was primarily added to gauge the performance of this new scintillating crystal. For the neutron fields, two different types of detectors were used. Eight NE213 liquid scintillators were installed to detect the fast, or high energy, neutrons. To detect the thermal (low energy) neutrons two ³He detectors were attached

to DANG, one with polyethylene shielding surrounding it. The reason two different types of neutron detectors are needed is described in detail in previous chapter. Figure 4.2 is an illustration of DANG, highlighting where each type of detector is located on the Aluminium structure.

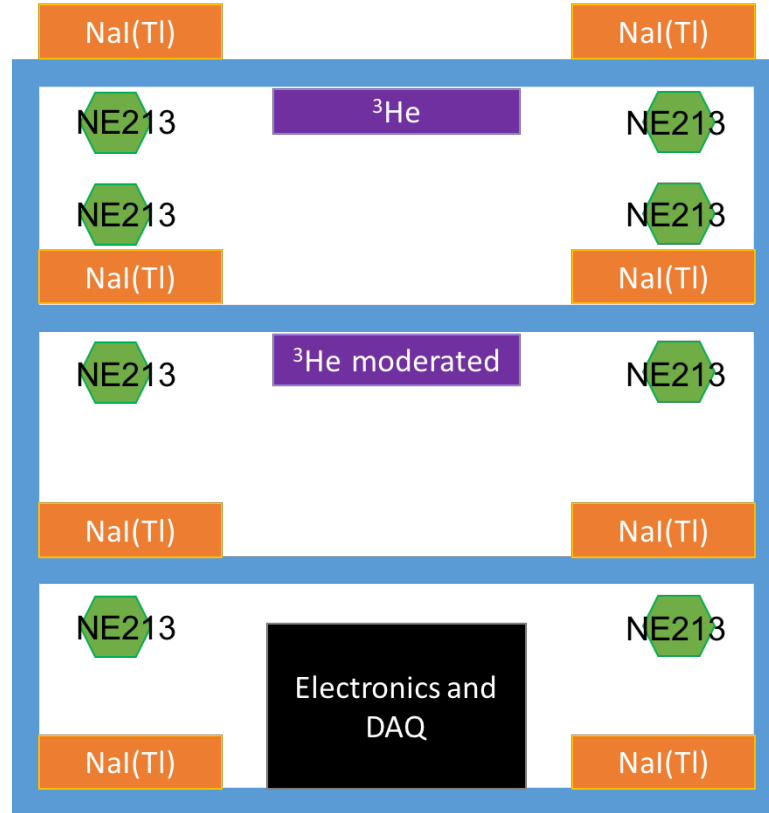


FIGURE 4.2: Figure outlining locations of DANG detectors on the structure.

4.1.1 Sodium Iodide Detectors (NaI(Tl))

To maximize the γ -ray efficiency, DANG uses large volume NaI(Tl) detectors. The dimensions of the detectors are 16" x 4" x 2", giving them a total active volume of 128 in^3 . The crystals are coupled with a 2" 9266B ET photomultiplier tube on one side [24] and a 276L Ortec low power photomultiplier base [25]. A spectrum taken with one of the NaI(Tl) detectors is shown in Figure 4.3.

The large active volume of the NaI(Tl) detectors and single PMT read-out while not optimised in regards to the energy resolution, is necessary to maximize the relative photopeak efficiency. The photopeak efficiency is defined as the proportion of γ -rays that deposit their full energy within the active volume of the detector. Figure 4.4 shows example spectra from one of DANG's eight NaI(Tl) detectors. These spectra were taken for 10 minutes and approximately 20 ft away from the reactor core. The peak located at 1.293 MeV during reactor-on is from the decay of ^{41}Ar , a by-product of the cooling

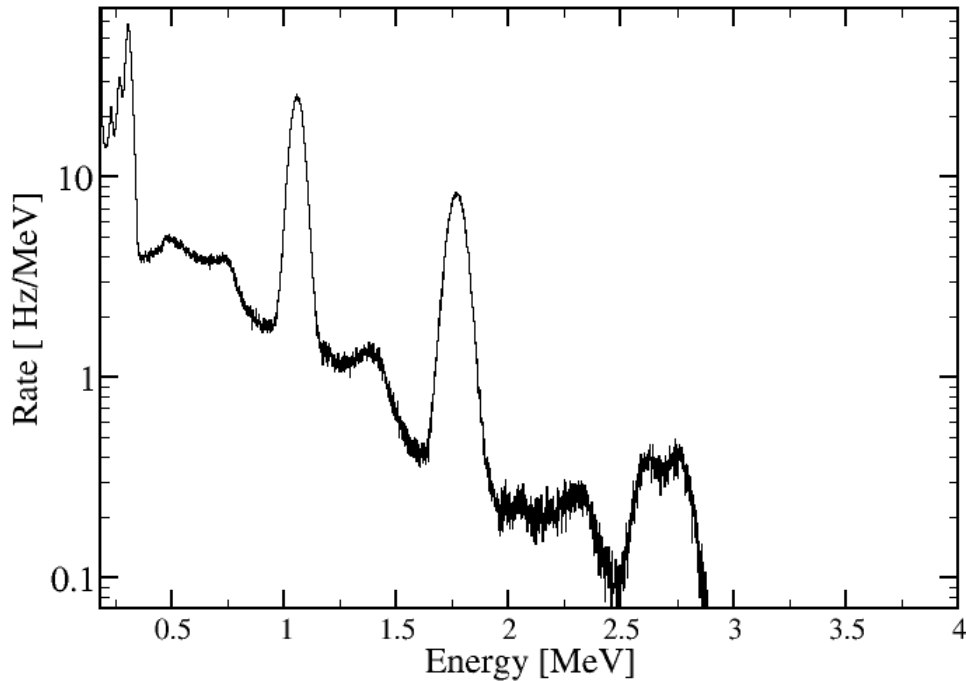


FIGURE 4.3: ^{207}Bi energy spectrum taken with a NaI(Tl) detector.

system for experiments at the Materials Irradiation Facility (MIF). The higher lying lines from 4-8 MeV are from neutron capture γ -rays[14]. The observation of a photopeak from neutron capture γ -rays is the result of the excellent γ -ray photo-peak efficiencies of these detectors.

The large photo peak efficiency and overall high efficiency of the NaI(Tl) detectors combined with the flux fields with the reactor on results in trigger rates over 100 kHz per detector. Such large trigger rates can have a significant effect on the resolution of the detectors. This effect is seen in the spectrum as not only a broadening of the resolution, but also as a gain shift of the peak centroids. This is most likely the result of high rate effects on the photo-multiplier tube causing large anode current and pile-up effects[26]. A systematic study of the performance at different trigger rates and detector voltages was undertaken. At lower voltages, the absolute height of the energy pulse is smaller. This effectively lowers the effect of pile-up at the cost of the resolution performance of the detector. The rate effects are illustrated in Figure 4.5. A high voltage of +1000V was chosen to produce an acceptable resolution minimising pileup effects.

A custom PMT base designed by Berkeley Electronics was attached to a NaI(Tl) detector and tested at various rates and voltages. These bases were developed by Lorenzo

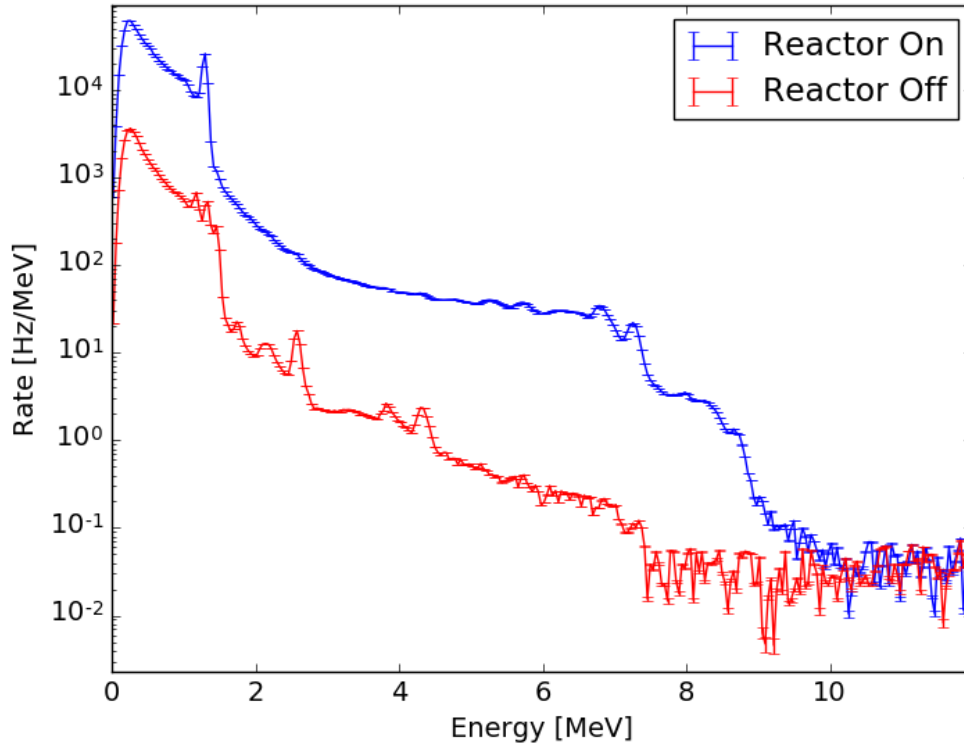


FIGURE 4.4: γ ray energy spectrum taken with a NaI(Tl) detector on the DANG array at the reactor, during the reactor-on and reactor off. The peaks seen in the 4-8 MeV region during reactor-on are the result of neutron capture gamma rays.

Fabris for the COHERENT collaboration[27]. These PMT bases were designed to operate in high flux radiation fields and to provide a low noise baseline. The test was conducted with both the new base and the original base attached to the detectors[25]. Calibration sources ^{207}Bi , ^{60}Co , and ^{137}Cs were used to probe the detectors' energy resolution (FWHM) at various distances from the detectors to observe different rates. The data acquisition system for this test was Caen's DPP-PSD software[23].

The energy resolution of the NaI(Tl) detectors with the new bases improved by 3-6%. Comparison of the gain shifts could not be clearly determined using this test method. This was due to indistinguishable peaks in the spectrum of the original bases at high rates. Figure 4.6 plots the energy resolution of the new and old bases at a variety of source energies and voltage settings. The trigger rate was not that high when only using the ^{207}Bi source, therefore rate effects were not prominent. Both the new base and the old base decrease in energy resolution as voltage decreases. As well, the new base has almost consistently better energy resolution at a given voltage.

While upgrading the PMT bases on the NaI(Tl) detectors is being considered for future measurements, the timeline to complete this falls outside of the current work.

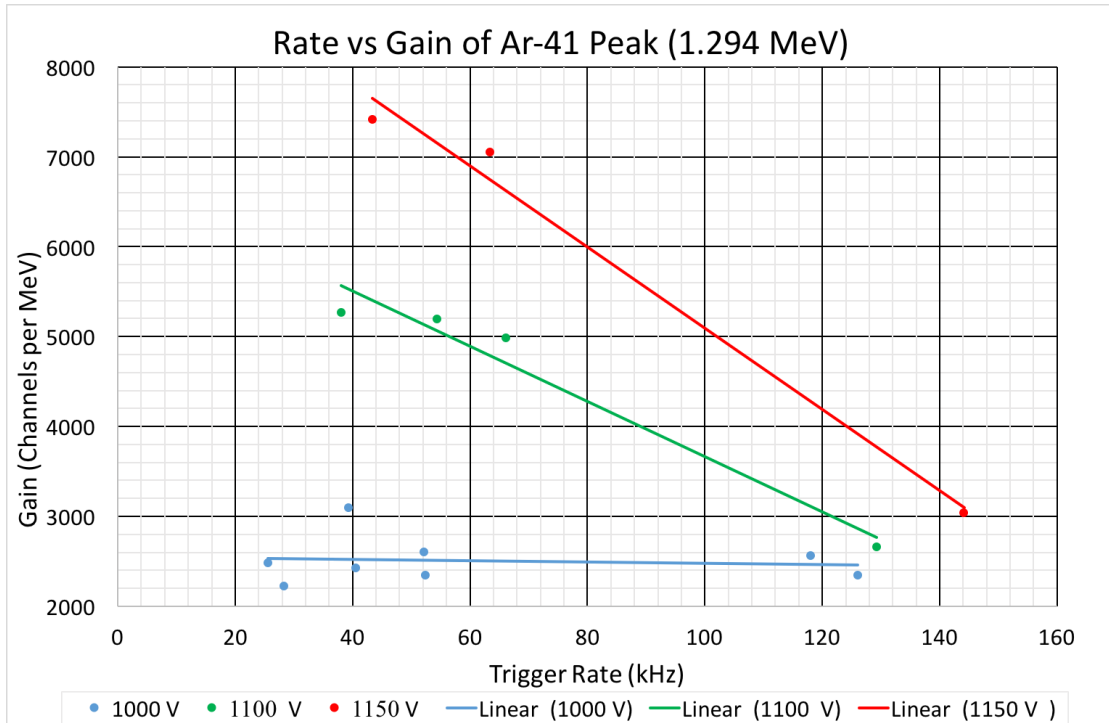


FIGURE 4.5: Rate versus the gain of the ^{41}Ar gamma peak in a NaI(Tl) detector. These measurements were conducted inside the experiment room at HFIR. The trigger rate was varied by changing the distance of the detector from the source of ^{41}Ar .

Aside from the overall rate effects of the NaI(Tl) detectors, the individual intrinsic efficiency of each detector was also considered. Understanding the intrinsic efficiency is important to check if each element is operating optimally and provides a quantitative understanding to the differences in performance of the eight detectors. The intrinsic efficiency is defined in Equation 4.1 as:

$$\epsilon = \frac{N_{\text{pulses measured}}}{N_{\text{radiation incident on detector}}}. \quad (4.1)$$

The efficiency measurements were obtained using ^{56}Mn and ^{24}Na sources produced in HFIR's core. ^{24}Na has two well spaced γ -ray peaks allowing for an easy calibration and ^{56}Mn has three well spaced γ -ray peaks, covering a substantial portion of the energy spectrum and making them suitable sources. Additionally, each source could be produced quite strongly at the in-house facility and then used immediately. Both sources had their activity measured and verified at the time of creation in the Neutron Activation Analysis lab at HFIR with a well characterised HPGe detector. The sources were then immediately used for a number of 10 minute measurements. The peak counts and calculated flux were used to determine the intrinsic efficiency of each detector. The intrinsic efficiency varied from detector to detector and remained within the range of 25-43%.

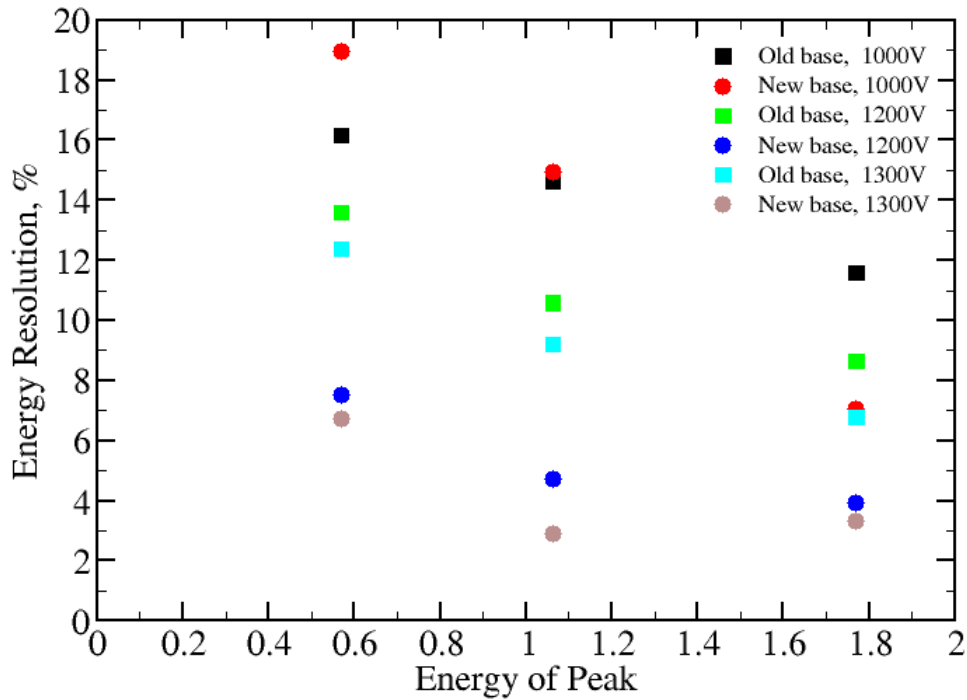


FIGURE 4.6: FWHM energy resolution as a percentage versus the energy of the gamma peak measured. These measurements were all taken with the same NaI(Tl) detector.

Detector Number	Intrinsic eff. (%)	Resolution Reactor on (%)	Resolution Reactor off (%)
NaI ₈	0.4108	5.91	5.98
NaI ₉	0.4327	5.80	5.43
NaI ₁₀	0.2483	8.28	4.88
NaI ₁₁	0.2784	5.88	5.42
NaI ₁₂	0.3996	6.12	5.52
NaI ₁₃	0.4018	5.77	5.63
NaI ₁₄	0.3732	5.67	4.86
NaI ₁₅	0.4269	5.78	4.98

TABLE 4.1: Intrinsic efficiency and resolution of the 1.294 MeV line from the decay of ⁴¹Ar for the Reactor on column and the 1.332 MeV line from the decay of ⁶⁰Co for the Reactor off column for each of DANG's 8 NaI(Tl) detectors.

The relatively long half life of ²⁴Na allowed for measurements to be conducted after the reactor had shut off. A significant drop in the intrinsic efficiency of the ²⁴Na γ -ray peaks was observed in every detector during reactor on period, decreasing as much as 80% from the nominal measured intrinsic efficiency. The cause of this was identified as an bug in the readout method of the digitizer in the data acquisition system ORCHID[28]. After

Detector Number	Correction Factor
NaI ₈	1.39(4)
NaI ₉	1.39(6)
NaI ₁₀	-
NaI ₁₁	1.13(3)
NaI ₁₂	1.30(3)
NaI ₁₃	-
NaI ₁₄	0.95(5)
NaI ₁₅	1.05(6)

TABLE 4.2: Correction factors for the rates observed in individual NaI(Tl) detectors to compensate for the observed deadtime effects caused by the bug found in the DAQ. Unfortunately, correction rates could not be extracted for NaI₁₀ and NaI₁₃.

comparing old data to a corrected set of rates, approximate correction factors were found for the rates. These corrections are displayed in Table 4.2.

It is expected that after the dead time correction has been made, the intrinsic efficiencies will be similar for reactor on and reactor off.

4.1.2 CeBr₃ Detector

During the course of this research project, a new scintillating detector, CeBr₃, was obtained by the lab for testing. This detector was installed on DANG in order to explore its performance and so that direct comparisons could be made to the NaI(Tl) detectors. An example spectrum taken with the CeBr₃ detector is shown here as Figure 4.7.

The CeBr₃ detector crystal has a diameter of 2" and is 2" tall. It was attached to the frame in the location shown in Figure 4.8. While the detector was only used for a short period, it was hoped to provide a more detailed, high resolution γ -ray background spectrum of the room.

The noise characteristics of the detector were inspected from waveforms captured by its associated digitizer. One such capture is presented here as Figure 4.9. One can clearly see a "ringing" on the output pulse from the signal. The cause of the "ringing" is currently understood to be due to an impedance mismatch between the cable attached to the detector and an adapter for the digitizer[16].

The ringing observed on the input signal is considered noise on the spectrum. Noise on the spectrum can have a number of negative effects on the measured energy. One negative effect is creating false leading triggers, causing the digitizer to convert the

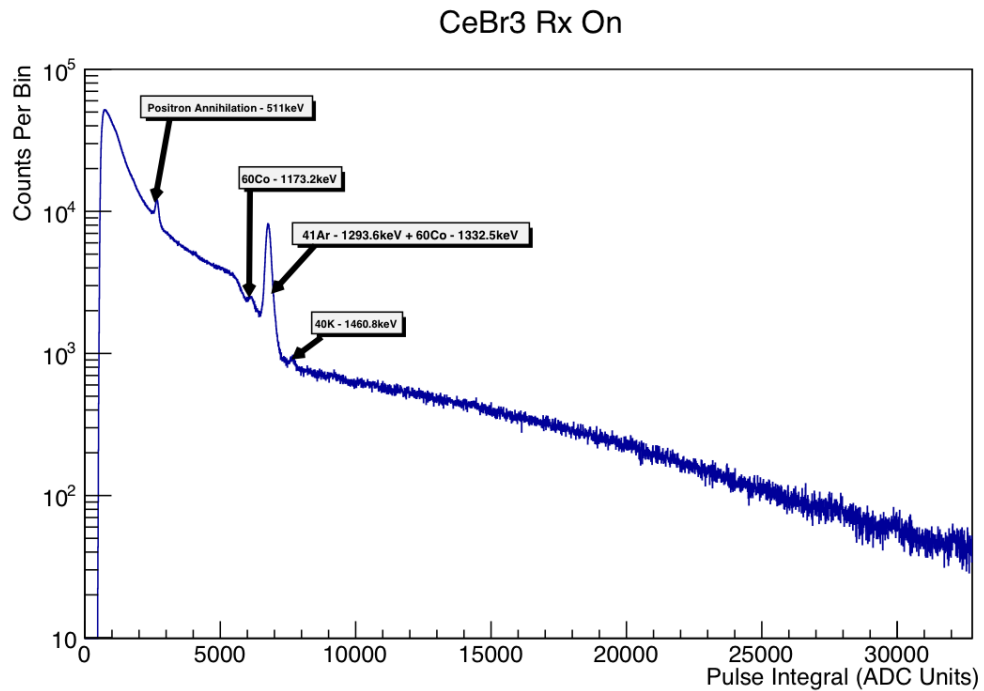


FIGURE 4.7: Spectrum taken from the CeBr₃ detector when the reactor was on. There is a clear increase in resolution in the ⁴¹Ar peak in this spectrum compared to Figure 4.4.

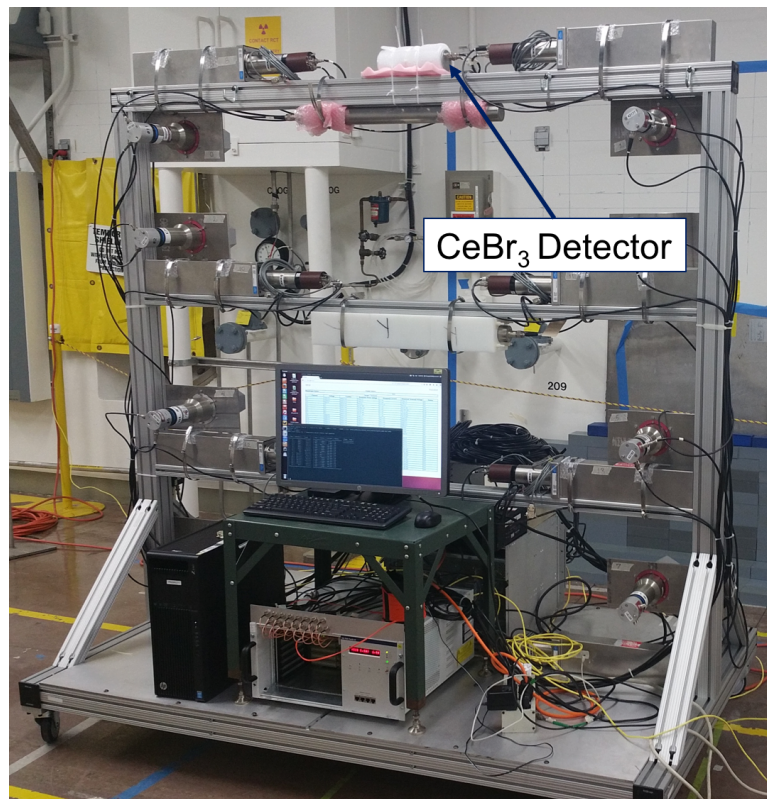


FIGURE 4.8: Image highlighting the CeBr₃ detector attached. Foam was used to protect the detector from strain and did not attenuate γ -rays entering the crystal.

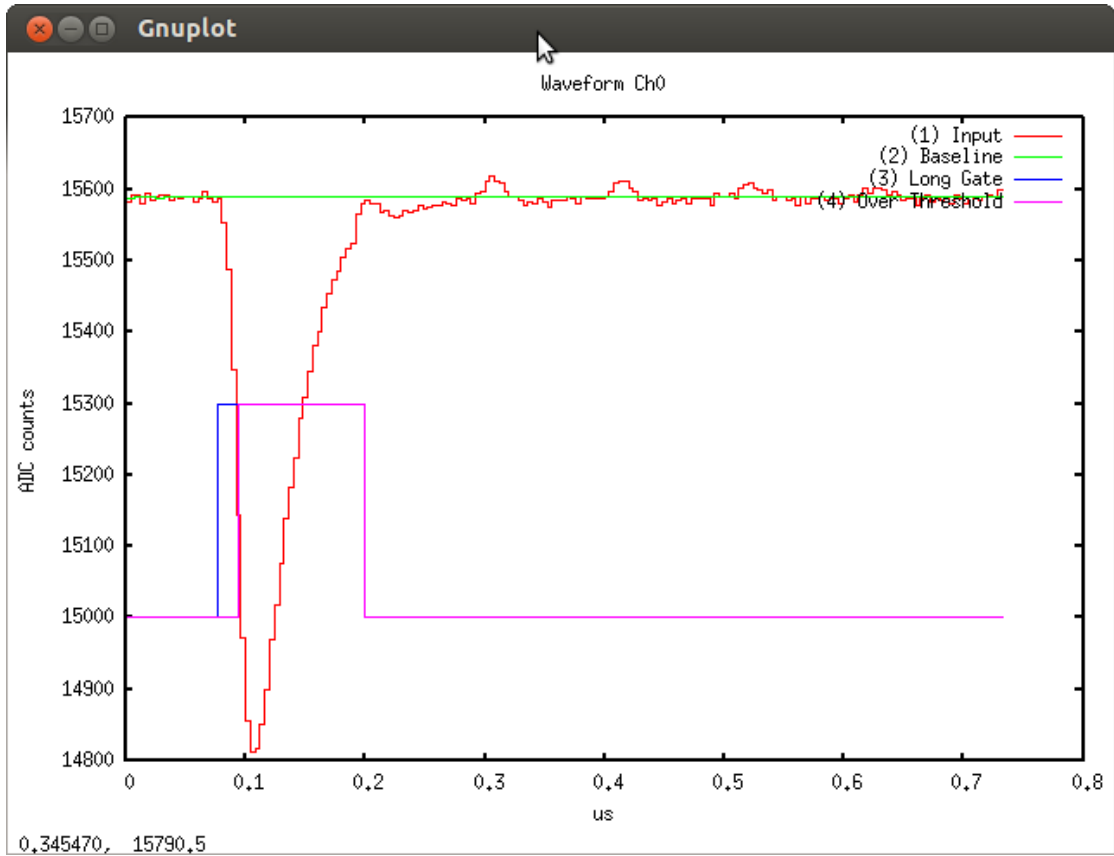


FIGURE 4.9: Pulse taken from the CeBr_3 detector. Evidence of small ringing can be seen in the tail of the pulse.

baseline to an energy output, i.e., creating low-energy noise. Fortunately, the overall amplitude of the reflection was found to be significantly smaller than the size of the total pulse, therefore these effects resulted in insignificant amounts of signal degradation.

Ultimately, the spectrum taken with the CeBr_3 detector was not significantly different from what was observed in the $\text{NaI}(\text{Tl})$ detectors. The CeBr_3 detector had a smaller efficiency for higher energy γ -rays and less detail in the spectrum. This is most likely the result of the small photopeak efficiency in the 2x2 detectors. The small size results in many of the interesting higher energy γ -rays only deposit a fraction of their energy inside the crystal. As well, most of the measured radiation in the room is from down-scattered γ -rays therefore would not have peaks visible in the energy spectrum.

4.1.3 NE213 Detectors

In order to detect the fast neutrons created while the reactor is on, DANG is equipped with eight NE213 liquid scintillator detectors. Each of the NE213 detectors has an active volume of 1.2 litres. This volume is attached to a 3 inch XP4312 PMT from Photonis[29] with a Photonis VD 123K base[30]. An image of the detector can be seen in figure 4.10.



FIGURE 4.10: Image of NE213 fast neutron detector as used on DANG.

A common challenge when detecting fast neutrons is being able to distinguish a neutron event from a γ -ray interaction. The resulting ionization of a scintillator particle looks very similar in most detectors. When using the NE213 detectors, pulse shape analysis can be done event-by-event to discriminate between γ -ray and neutron events[31].

The particles are identified by plotting a long and short charge integration, Q_L and Q_S , which separates the different particle types into two distinct bands. A detailed discussion of this discrimination process is given here in Chapter 3. The optimal values of Q_L and Q_S were determined for each NE213 detector using a ^{252}Cf source. ^{252}Cf is a fission source which produces neutrons and a wide variety of γ -rays on the order of MeVs from the various daughter products. Figure 4.11 is an example spectrum produced where the neutron events can be seen in the upper band and the γ -ray events are seen in the lower band.

Figure 4.12 is a spectrum of data collected while the reactor core was operational. The large flux of γ -rays produced by the reactor causes a distortion seen in the plot and blurring effect between the the neutron and γ -ray bands. This is most likely a pile-up effect.

To combat these degraded spectrum, the NE213 detectors were calibrated using an AmBe source . The AmBe source releases neutrons and γ -rays within the MeV range. Using the higher quality spectrum, careful gates were placed around the known neutron band. These same gates were then used to cut out γ ray measurements from reactor on

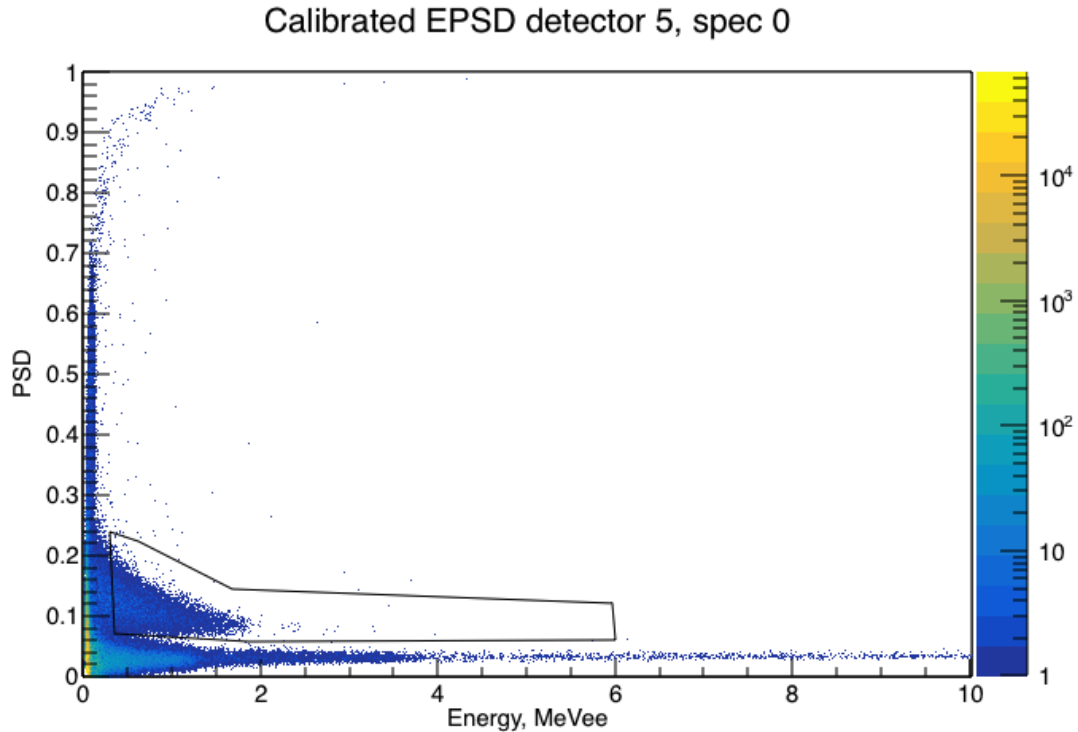


FIGURE 4.11: Ten minute measurement taken with an AmBe source. Black line is the gate around the neutron signals in the range of 0.3-6 MeVee. The upward sloping line is the result of clipping in the detector[16].

spectra, isolating fast neutron counts where the neutron band was not clearly observed. Figure 4.11 is an example spectrum taken from this calibration. The neutron cuts can be seen around the neutron band as a black line. The separation of the two tails in the low energy part of the spectrum can be seen at approximately 0.3 MeV. Neutrons were cut off at 6 MeVee in the high energy part of the spectrum as this is where clipping starts to occur in some of the NE213 detectors.

4.1.4 ^3He Tube Detectors

DANG is equipped with two ^3He proportional detectors to effectively count present thermal neutrons. Both detectors have a nominal internal pressure of 10 Bar and are 2" in diameter and 24" long. Figure 4.13 is a diagram from [32] to show what a neutron energy spectrum looks like with a ^3He detector.

In contrast to the NE213 fast neutron detectors, the ^3He proportional counters directly detect the neutrons from a capture reaction that releases a proton. An image of a ^3He tube pulse is presented here as Figure 4.14.

To detect the charge collected from the proton's ionization trail, the ^3He counters are directly connected to a Canberra Preamplifier that in turn is connected to an Ortec

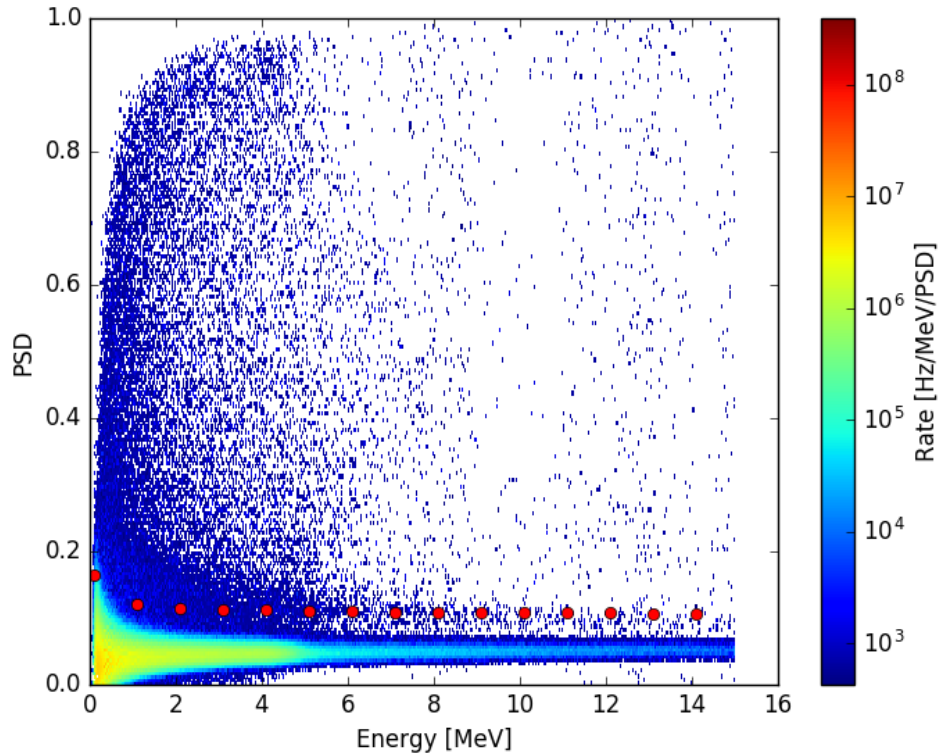


FIGURE 4.12: A spectrum of data collected with the NE213 detector while the reactor was on. There is a large γ flux in the detector and combined with degraded signal quality from the detector makes it difficult to identify which areas of the spectrum should be counted as either neutron or γ -rays.

Spectroscopy Amplifier. The electronics layout of DANG is shown here in Figure 4.15. These electronics are sensitive and occasionally have started triggering on noise after being jolted.

The mechanism used to detect thermal neutrons in ^3He detectors cannot clearly define the neutrons' initial energy or direction (refer to chapter 3). This mechanism is however very good for discriminating between γ -rays and neutrons. The probability of a γ -ray interaction in ^3He is so small, all the counts can be determined as neutron interactions. A study was conducted to measure the sensitivity of the detectors to γ -rays to justify this claim. Data was collected from a strong ^{127}Cs source attached to the center of the unmoderated ^3He tube during a reactor off period. The placement of the ^{127}Cs source relative to the detector caused a γ -ray flux significantly higher than the flux during reactor on. The rate in the ^3He tube was measured in 10 minute intervals with and without the source present. The increase in counts due to the γ flux was found to be less than 1% of the total reactor on rate. This justifies the above claim that the ^3He tubes are insensitive to γ radiation.

^3He cross section with neutrons increases as the kinetic energy of the neutron decreases. Therefore, one of the detectors has a 1 inch polyethylene shielding surrounding it. Polyethylene has a high cross section with neutrons. Thus, the polyethylene will slow some of the faster neutrons, increasing the likely hood of those neutrons being counted by the ^3He tube. This shielding package was custom designed by drilling a 2.05 inch diameter hole through the center of polyethylene bricks in which the ^3He tube was inserted. The bricks are then threaded together with polyethylene rods, maintaining a consistent material in the shielding. This removes the chance of any shielding material becoming activated over time. Figure 4.16 highlights the position of two ^3He tubes on DANG, highlighting the moderated detector, encased in the polyethylene shielding.

4.2 Electronics

The electronics, data acquisition system, and power supply for DANG were all installed on DANG's mobile aluminium platform. This minimizes set up time of the electronics as DANG is moved to various locations around HFIR. The arrangement also provides

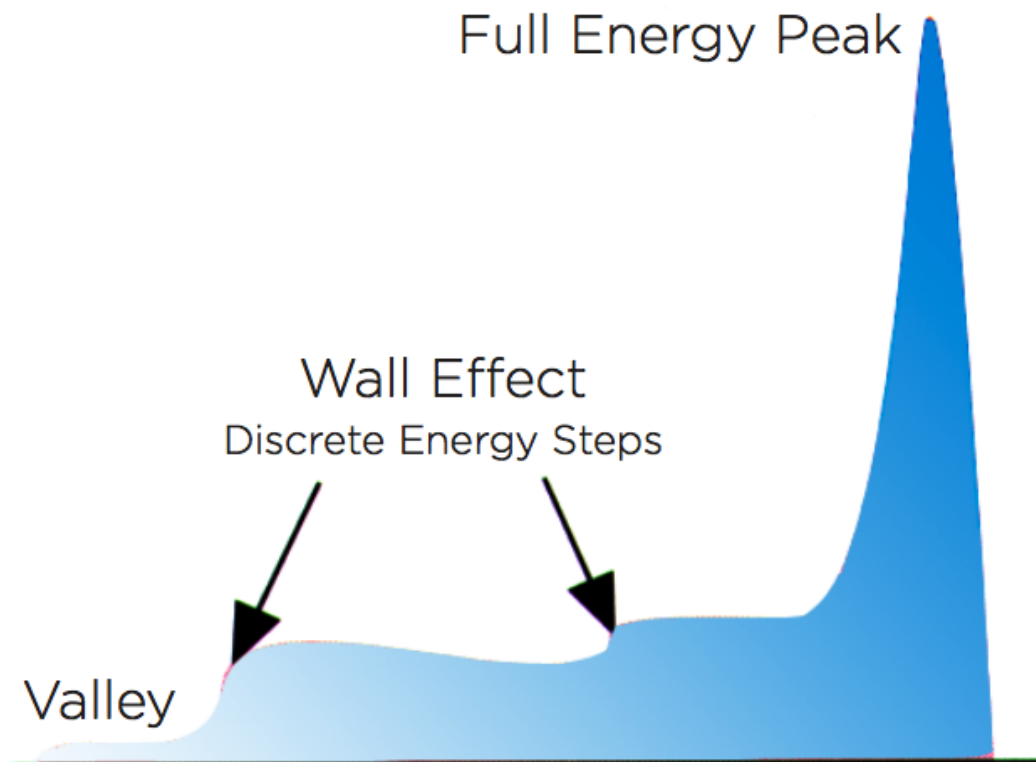


FIGURE 4.13: Diagram of a ^3He spectrum using a multichannel analyser[33].

a cable management system to protect the various connections in the array. The individual electronic modules used for the array were carefully selected for their optimal performance and relevance to the PROSPECT collaboration.

Additionally, the detectors on DANG are powered by an MPOD high voltage crate and card. MPOD is a universal multichannel high voltage system that can be controlled remotely through a computer interface[34]. An ethernet connection is used to control and monitor the voltage from a server running on the DAQ computer, allowing for easy controlled access to the voltage of the detectors. Figure 4.17 is an image of the MPOD mounted on the mobile aluminium platform which holds DANG.

4.2.1 CAEN VX1730 Digitizer

The Caen VX1730 16-channel, 500 MS/s digitizer was used for converting the output signal from the various detectors on DANG into a digital charge and time[23]. A resolution of 14 bits per sample maximizes the energy resolution and pulse shape discrimination of the detectors in DANG. A study of how an increased number of bits improves energy resolution is shown in Figure 4.18. In this figure, Caen uses a scintillator to generate figure of merit values for the energy resolution for different bit sized digitizers[23]. From

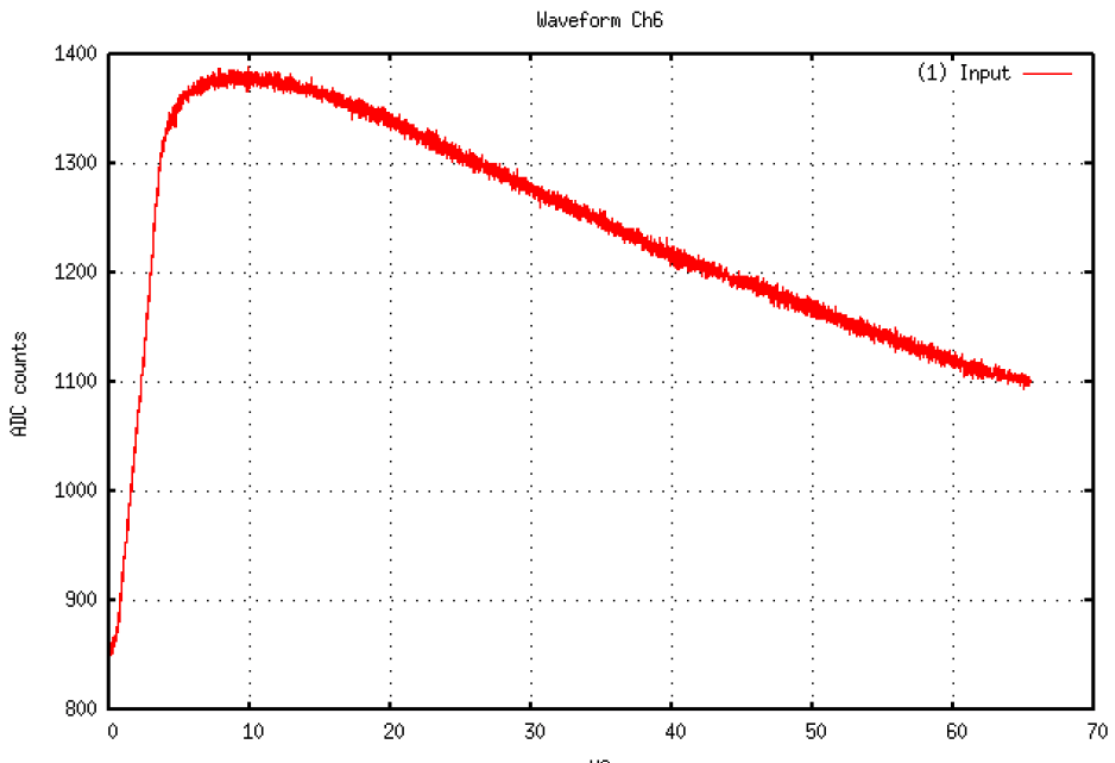


FIGURE 4.14: Pulse shape of a thermal neutron captured in the one of the ^3He detectors.

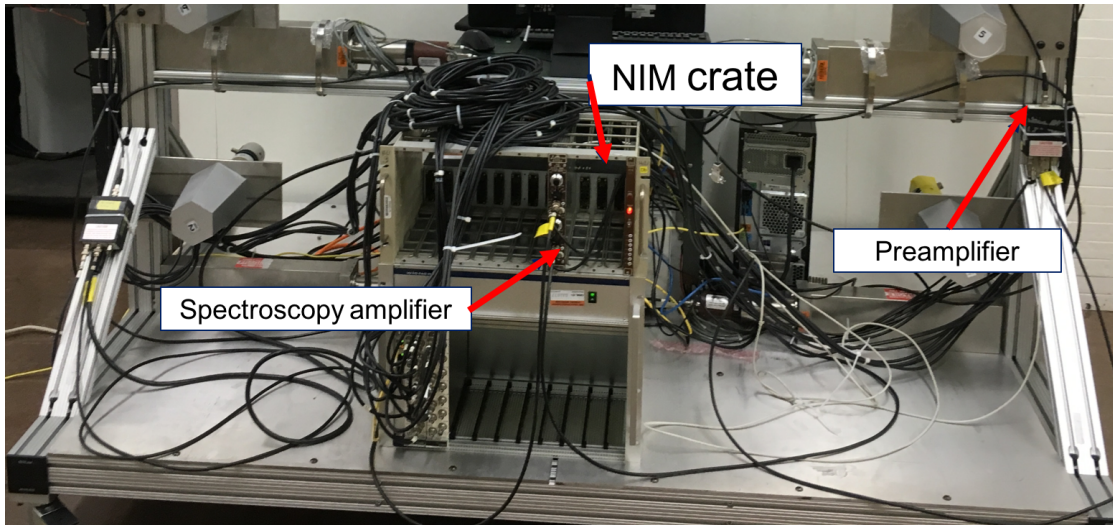


FIGURE 4.15: Image taken of DANG highlighting the supporting electronics for the ^3He tubes.

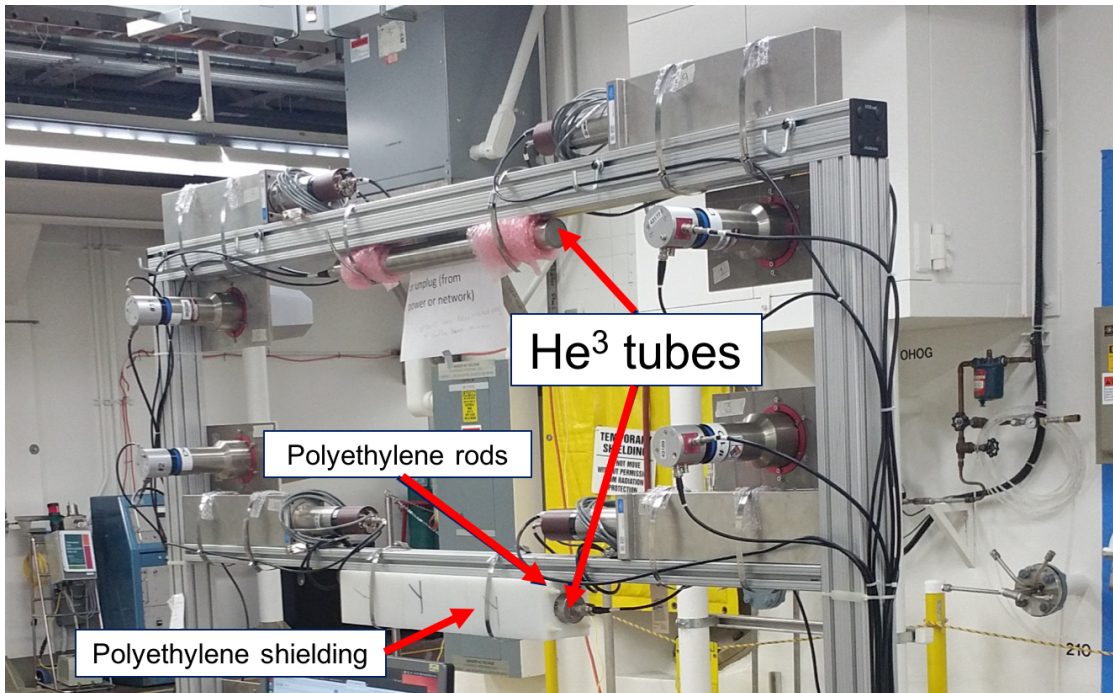


FIGURE 4.16: Image was taken of DANG highlighting the polyethylene shielding surrounding the moderated ^3He tube.

this study, it is clear that the 500 MS/s, 14 bit size digitizer provides the most effective readout of a detector signal, maximising on the potential resolution of the measurement.

The digitizer itself is powered through a VME-64X[35] crate. Data from the digitizer is read out through an optical link and fed into a computer running the DAQ software. The digitizer input slots are high density MCX connectors, with all 16 channels having independent connections on its front panel. The digitizer, VME crate, and DAQ computer are highlighted in Figure 4.19.

The output of the detectors is a standard BNC (Bayonet Neill-Concelman) connector. This connector is used on a large variety of electronic modules and detectors[16]. A BNC to MCX adaptor built by Adafruit was selected to create a single adaption from the BNC cables into MCX cables, minimising the introduction of noise. A patch-panel was constructed and mounted to the VME crate to manage the number of cables which needed to be converted. Not only does the patch-panel help organize the individual cables as DANG is moved from location to location, but it also provides stress relief for the connections, effectively extending the usable life time.

The Caen VX1730 digitizer was also selected for its relevance to the PROSPECT detectors. The full-scale experiment is planning on using a number of the Caen VX1725 digitizers for the individual cell readouts[36]. The two digitizers are nearly identical, with the only difference being the VX1725 has a slightly lower sampling rate of 250 MHz. Getting familiarised with the VX1730 digitizer data readout, triggering scheme,

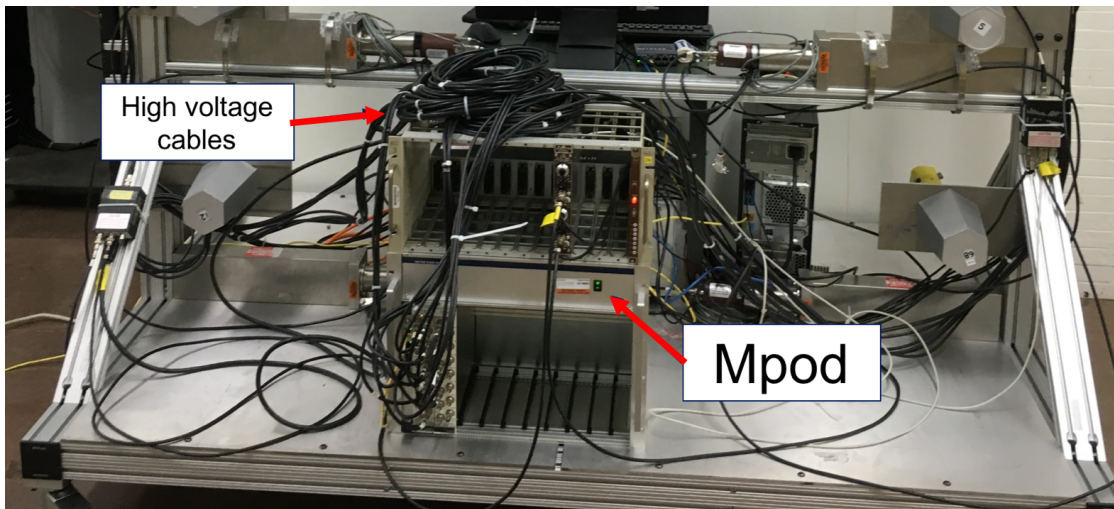


FIGURE 4.17: Image of DANG highlighting the location of the MPOD high voltage supply and the mobile support structure which supports DANG.

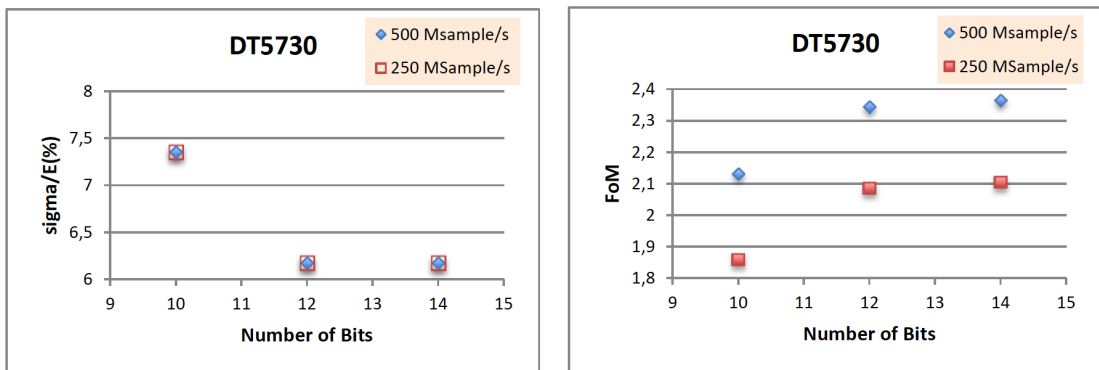


FIGURE 4.18: Plot displaying the energy resolution, as determined from the 511 keV Compton Edge (left panel) and FoM (right panel) for different sampling rates and digitizer resolutions. For details see reference [23].

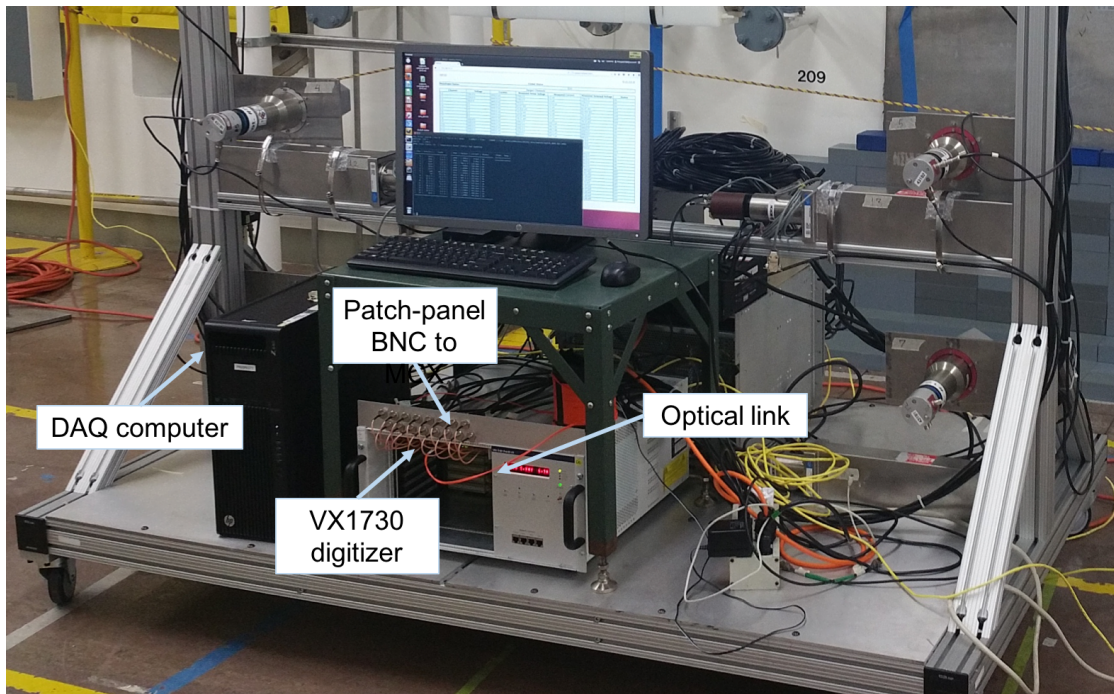


FIGURE 4.19: Image of DANG highlighting the digitizer and input and output connections.

and energy filters should greatly ease the initial deployment of the PROSPECT components. It has also been beneficial to the collaboration to gauge the performance of the Caen circuitry in the high neutron and γ fields present while the reactor is on. Such fields can cause large amounts of ionizing radiation on or near the electronics, which may in turn have an adverse effect on their performance.

The Oak Ridge Conditions at HFIR DAQ (ORCHID) is being developed to read and reconstruct events from the various detectors of DANG. This custom data acquisition system utilises some of the unique and accurate timing properties made available by the Caen VX1730 digitizer. Gaining experience in handling the data read from the digitizer as well as becoming familiar with these unique features provided by the Caen boards will add experience and expertise to the PROSPECT collaboration for the ambitious full scale experiment.

Chapter 5

Background Measurements

In the early stages of the PROSPECT experiment, the collaboration conducted background surveys at various reactor facilities, leading to the selection of HFIR as the future experimental site[37]. However these surveys also highlighted a large gamma flux and presence of thermal and fast neutrons present at HFIR from the reactor and cosmic backgrounds. The PROSPECT collaboration concluded that these fields could be mitigated by conducting a careful measurement and characterisation of the background fields. These measurements could then provide feedback to active and passive shielding designs around PROSPECT itself. Simulations could also be used to estimate the background radiation inside the full scale PROSPECT detector, managing the backgrounds to fall within the necessary bounds to ensure the PROSPECT's success.

5.1 Aims of Survey

The present work was conducted in two main studies; looking at the spatial variations and looking at time dependencies in the radiation fields. Potential sources for some time and spatial fluctuations have been identified using the knowledge of HFIR's operation, structure of the facility and experiments occurring in other parts of the building.

The aims of the present work include:

- Detailed characterization and quantification of the strength and location of γ -ray and neutron fields throughout the experimental area
- Detailed mapping of the γ -ray and neutron fields as a function of time through the HFIR reactor cycle
- Identifying hot spots of radiation within the experimental area and identifying potential sources

This information will help develop the best possible active/passive shielding arrangement and provide a baseline for expected background fields during PROSPECT's operation.

5.2 Method of Measurement

Background radiation measurements have been made in the experiment area with a variety of detectors and under a number of different environmental conditions. These environmental conditions include the reactor being on and off, temperature fluctuations and the introduction of the MIF experiments, which doubled the observed γ -ray fields in the room[38]. The individual measurements of the background fluxes ranged over many months and conditions were susceptible to change. Therefore ensuring consistency was key so the measurements could be compared. Consistency checks entailed mapping the experimental area to ensure precise and repeatable measurement locations, minimization of position scans as a function of time to ensure a constant counting rate, and identical settings applied to each detectors on a run by run bases. Keeping some consistency between the measurements became a priority to make certain individual measurements are comparable.

5.2.1 Reactor Status

The reactor runs for cycles of approximately 20 days on followed by 20-60 days off. During the reactor-on cycle, there are a number of experiments occurring around and within the reactor, including neutron beam lines, Materials Irradiation Facility(MIF), reactor waste fuel storage and source irradiation (NAA). These experiments represent sources of radiation aside from the reactor core, creating a more complex background field in the experimental area than a simple $1/r^2$ dependency.

The background fields become more complicated as experiments start and stop while the reactor is on. For example, the neutron beam lines on the floor below are opened

and closed based on the specific experimental requirements[5], potentially providing a substantial varying source of background radiation with time[39]. Additionally, other experiments produce characteristic radiation as a by product of their operation. The MIF (discussed in more detail below) is a perfect example of this, as it produces an extremely strong source of ^{41}Ar , drastically increasing the γ -ray fluxes in the room.

Measuring the background produced from these sources across a reactor on/off cycle allowed us to probe the decay behavior of the produced radiation. While many of the background fields were found to be prompt, meaning once the reactor goes off, background fields from these sources also disappeared, some longer lived activity was located. Furthermore, cosmic background can be probed once the reactor is off[12].

5.3 Temporal Study

The background fields can fluctuate as a function of time during a reactor cycle. To further explore these fluctuations as a function of time, DANG was positioned within the volume the PROSPECT will occupy and left counting on all detectors. Data collected during this time was sorted into ten minute intervals, allowing for a detailed look of these fluctuations.

5.3.1 NaI(Tl) Results

Over the course of the temporal study, gain shifts were observed in the NaI(Tl) detectors. To overcome these shifts, each sorted ten minute data block was independently calibrate using well-known peaks observed in the background when the reactor is on and when the reactor is off. An example spectrum produced from one of these ten minute data blocks is shown here as Figure 5.1. In the spectrum, both the ^{41}Ar and ^{60}Co peaks are clearly seen for reactor on and reactor off respectively.

Variations and electronic interference are still observed the resulting spectrum which seemingly come and go as a function of time. Perhaps most note-able are "spikes" or "dips" which appear in the 9-10 MeV range in the NaI(Tl) spectrum (Fig. 5.2). This theory is supported in two ways: the "spikes" appear to correlate with count rate increases across the array, also observed γ -rays in this energy range are predominately from cosmogenic radiation and the cosmic background radiation has been proven constant with time[37]. An example of a "spike" in the high energy region is shown in figure 5.2 just before September 28. During the "spike", all of the energy bins have an increased rate, including the 9-10 MeV bin. These spikes and dips are most likely artifacts caused

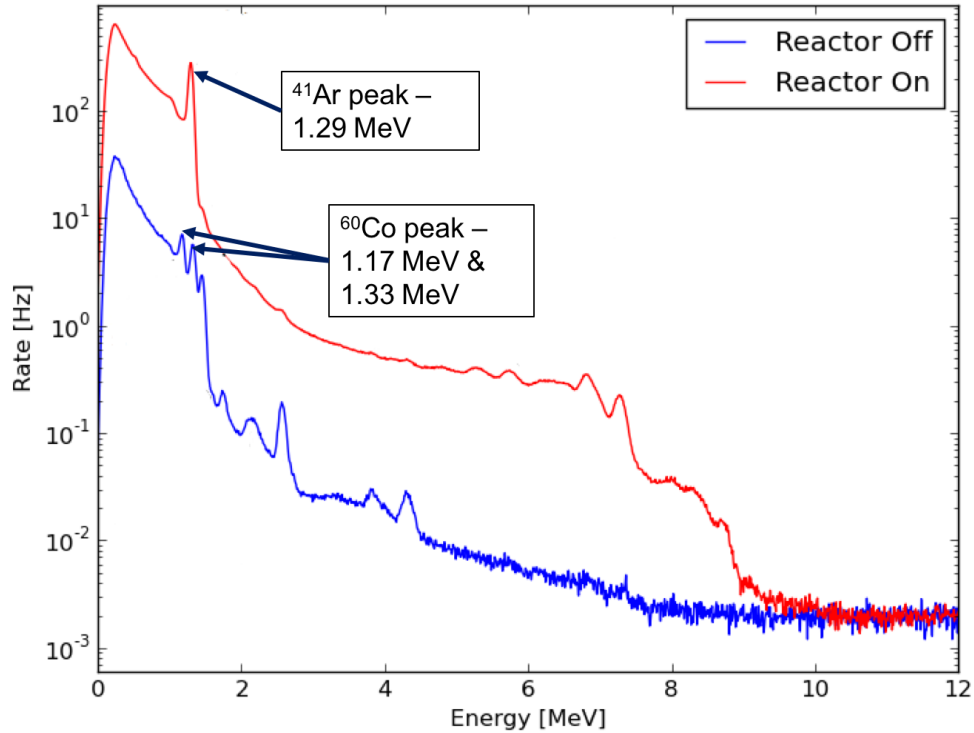


FIGURE 5.1: Spectra taken with an NaI(Tl) detector during reactor-on and reactor-off with error bars. Clear neutron-capture γ -rays can be seen in the high energy region of 4-8 MeV.

by timing issues in the digitizer or the DAQ. Currently the custom ORCHID is being developed to adjust and mitigate such effects[28].

The eight NaI(Tl) detectors are placed across the array at a variety of different heights. Comparing the measurements from the different detectors yields some interesting results. For example, the detector least effected by rate effects is Detector 14; one of the detectors farthest from the MIF and 11" from the ground. The rates from this detector over the reactor-on cycle 468 are displayed in Figure 5.2. The rates were calculated in 1 MeV energy bins across the spectrum, where each colored line in the graph represents a different energy bin. Separating the rates into energy bins not only provides more detailed information about the fluctuations but also makes it easier to associate which reactor related operation it comes from. For example, the γ -rays in the 5-7 MeV range are mostly from neutron captures in the building's material. The lower energy γ -rays in the 0.1-3 MeV range could be from either down-scattered neutron capture γ -rays or from decaying activated material like ^{41}Ar and ^{60}Co .

A known hotspot for background radiation at HFIR is neutron beamline HB-3[38]. This beam line is a diffractometer and can be opened and closed by experimenters[13]. Most of

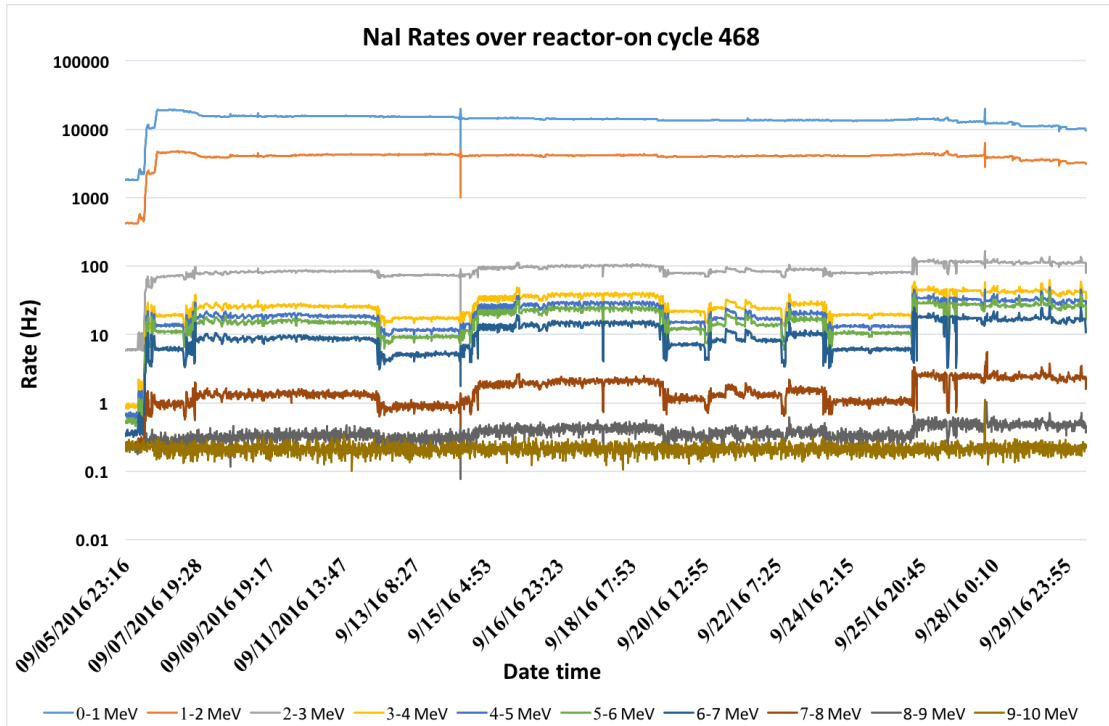


FIGURE 5.2: Reactor-on rates over one cycle with a NaI(Tl) detector (DANG detector 14), 11” from the experiment room floor. The different color lines correspond to energy bins, where counts were summed in order to calculate the rate. Values for the different lines are on the bottom of the graph.

the information about the experimental operation of this beamline is recorded in the run log[39]. Some bumps and troughs seen in the rate measurements correlate with these run logs. For example, the rise and fall of a small plateau observed on 9/21/2016 correspond perfectly with Experiment 556 scan 16 in HB-3[39]. There was a 30% increase in rate from the baseline before the experiment to during the experiment. Figure 5.3 expands the timeline of the rates around Experiment 556 start and stop. Both the NaI(Tl) and ^3He detector during this experiment experience an increase in rate, highlighting that this DANG is sensitive to HB-3 operations, through both neutron and γ ray detection.

Troughs in the γ -ray rates are also found to correlate with the operation of HB-3. A trough seen on 9/26/2016 was also found to correspond with a HB-3 scan that was aborted and switched closed, where a 47% drop in rate is observed in the 3-8 MeV region from the baseline immediately after the beamline was closed.

An example of the background flux decay in the room immediately after the reactor is switched off is presented in Figure 5.4. Once again, features in the graph are well correlated to reactor operations. Immediately after the reactor is switched off, we see characteristic decay curves we would expect from isotopes produced while the reactor is on. Interestingly enough, different energy ranges appear to have very different half-lives, indicating a wide range of isotopes with varying Q-values are most likely present.

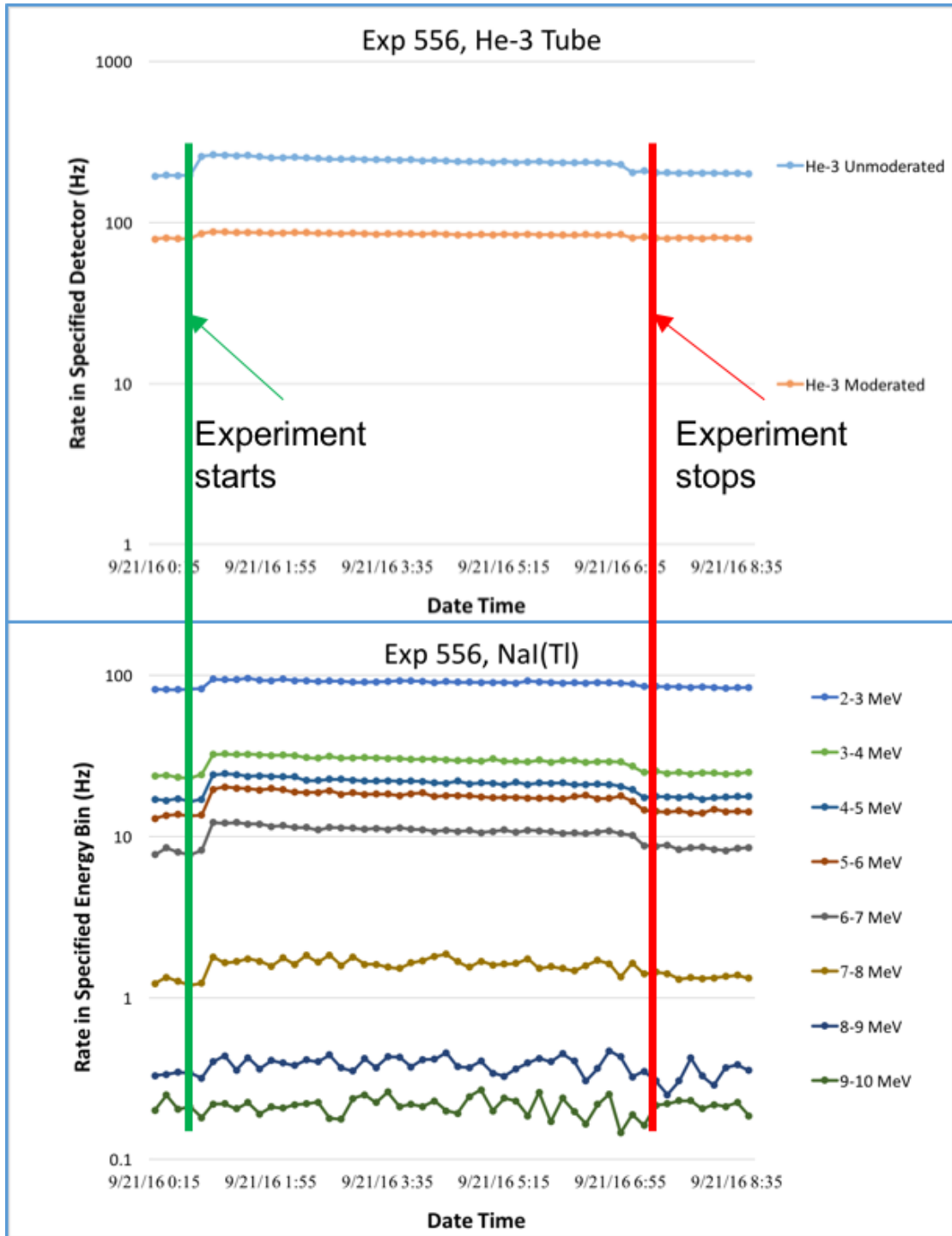


FIGURE 5.3: Rates seen in the NaI(Tl) detector 14 and the ^3He tubes during HB-3's Experiment 556. This correlated event highlights that DANG is sensitive to the neutron beam line operations on the floor below.

Furthermore, two clear spikes can be seen around 01/10/2016. These spikes correlate perfectly with the fuel removal from the reactor core. After the reactor shuts off, the inner and outer fuel elements inside the pool are lifted out in sequence and moved to the spent fuel section of the reactor pool[5]. There also appears to be a second decay curve

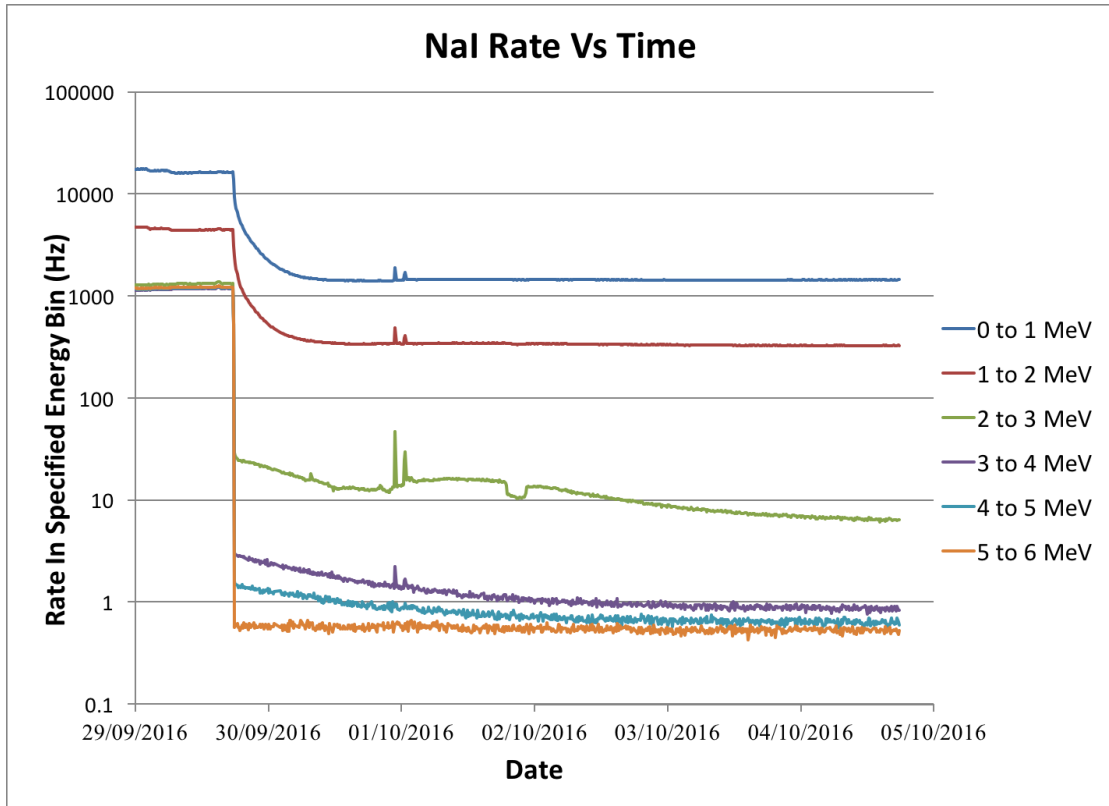


FIGURE 5.4: Measurements taken for a few days after reactor is shut off. Spikes clearly correlate with reactor operations in this period. The different color lines correspond to energy bins where counts were summed in order to calculate the rate.

after a small rise in the 2-3 MeV energy range between 01/10/2016 to 04/10/2016. This feature is expected to be activated ^{24}Na in the reactor pool. Tiny amounts of activated ^{24}Na in the reactor pool would have evaporated into the air and would have been distributed throughout the building. The dip is expected to be the result of a partial vacuum test in the pool room, drawing some of the activity out of the experimental hall temporarily.

This work has been successful in demonstrating a clear correlation of rates background flux with reactor and beam line operations. A full operating parser of HB-3 logs and identification of which of HB-3 operation effects the γ -ray rates falls outside the scope of the current work.

5.3.2 CeBr_3 Results

The CeBr_3 detector was incorporated in DANG for a few days during reactor shut down, the same time period as figure 5.4. The detector provided a good comparison to the fluctuation of rates seen in each of the NaI(Tl) detectors. Figure 5.5 shows the time evolution of the measured rates for different energy bins

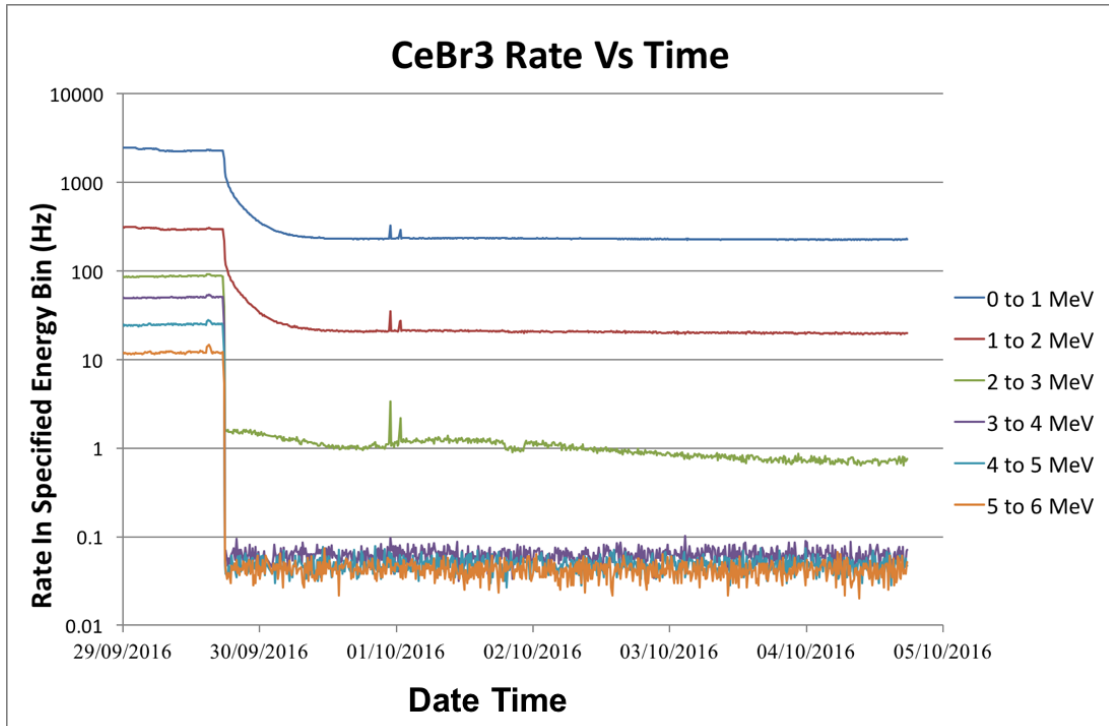


FIGURE 5.5: Measurements taken for a few days after reactor is shut off using the CeBr_3 detector. Spikes clearly correlate with reactor operations in this period. The different colored lines are energy bins where counts were summed in order to calculate the rate.

Similar features are seen with both the CeBr_3 detector and in Figure 5.4 with the $\text{NaI}(\text{Tl})$ detector. This provides even further evidence that the observed features are truly associated with reactor operations such as fuel removal and the exponential decay of the ^{24}Na as discussed above. Smaller differences are due to a smaller efficiency but these detectors do have a higher resolution than the $\text{NaI}(\text{Tl})$ detectors. Using a CeBr_3 detector may have the advantage of a higher energy resolution but the small photo-peak efficiency makes it plebeian for our background studies.

5.3.3 ^3He Results

As discussed in Chapter 3, the ^3He detectors are proportional counters therefore can only provide rate information on the thermal neutron fields. Two ^3He detectors were attached to DANG at different positions. One detector, moderated with 1" of polyethylene to thermalise neutrons, was mounted 50" from the floor, while the second (unmoderated) was mounted 75" from the floor. The rate as a function of time for these two detectors during reactor-on cycle 468 is presented in figure 5.6. The time scale and range in figure 5.6 is the same as previously shown for the $\text{NaI}(\text{Tl})$ detector in Figure 5.2. In Figure 5.6, there is an empty period from 09/14/16 to 09/20/16. This was due to

the detectors needed by another group and temporarily being removed from the the array. Consistently throughout the cycle, the unmoderated detector has had a larger trigger rate than the moderated detector. This is suspected to be due to the fact that the majority of the neutron flux is thermal and so the polyethylene is acting as an absorber rather than a moderator. The polyethylene therefore decreases the moderated detector's trigger rate relative to the unmoderated. This suggests that the majority of the neutrons in the area are thermal rather than epithermal.

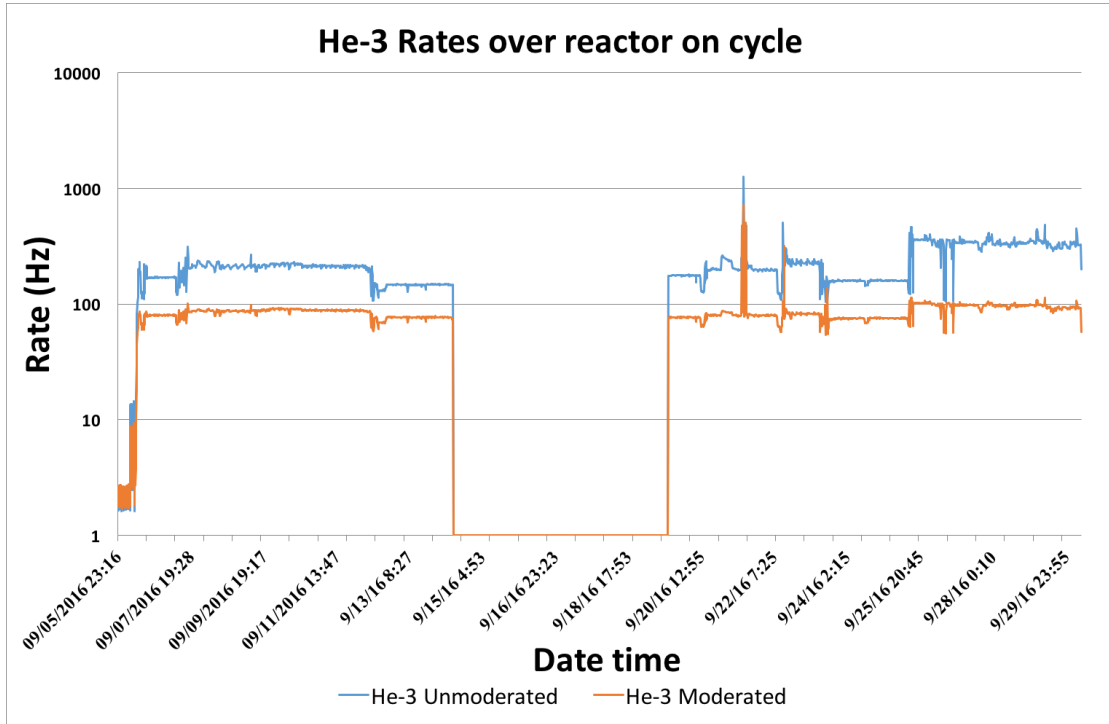


FIGURE 5.6: Measurements taken over a reactor-on cycle with the two ^3He detectors. The different colored lines represent the two different ^3He detectors, moderated (orange) and unmoderated (blue).

Clear fluctuations of rates are observed in ^3He detectors which correlate well with the NaI(Tl) and CeBr₃ (where data is available). Again a number of correlations can be found and associated with events in the HB-3 experimental logs[39]. The plateau seen in the NaI(Tl) detectors on 9/21/2016 is also seen in the ^3He detectors. As previously noted, this plateau corresponds with Experiment 556 scan 16. An illustration of this plateau and its correlation with the NaI(Tl) detector measurements is shown in Figure 5.3. During Experiment 556 scan 16, there was a 9% increase in rate in the moderated detector and a 25% increase in rate in the unmoderated detector from their respective baseline rates. Also like the NaI(Tl) detectors, there is a drop in rate on 09/26/2016 when an experiment in HB-3 was aborted. At this point, there was a 38% decrease in rate in the moderated detector and a 66% decrease in rate in the unmoderated detector from their respective baseline rates. Further research into the specific protocol of how

the HB-3 experiments are aborted is needed to best understand the true cause of these dips.

Interestingly, it appears that the ^3He detectors are more sensitive to the operation of HB-3 than the NaI(Tl) detectors. Additional drops in rate are seen in Figure 5.6 from other scans that were aborted in HB-3, one being on 9/20/16 that was not observed in the NaI(Tl) detectors. This is as expected as ^3He detectors are thermal neutron detectors and the HB-3 beam line emits predominately neutrons. On the other hand, the ^3He detectors are less sensitive to power fluctuations and conditions in the reactor. Unlike the NaI(Tl) rates in Figure 5.2, no step-like detail about the reactor turning on is seen in the 9/06/16 period, only a simple hike in rates. Again this is as expected as HB-3 is the largest contributor to fluctuating thermal background neutrons and the operation of HB-3 is prompt rather than a staggering increase like the powering of the reactor.

5.3.4 NE213 Results

The NE213 fast neutron detectors are susceptible to rate effects from both γ -rays and neutrons. Some methods used to mitigate these effects and pile-up as well as discriminate between incoming γ -rays and neutrons is discussed in Chapter 4. Cuts were made around the neutron to extract neutron rate measurements for this study in an attempt to isolate neutron counts. Figure 4.11 is a 2D neutron spectrum illustrating these cuts. Similar to the NaI(Tl) detectors, energy calibrations were also performed for every 10 minute data bunch to combat gain shifts and rate effects. While the reactor was on, the detectors were individually calibrated using the Compton edge of the ^{41}Ar peak. However, unlike the NaI(Tl) detectors, the NE213 detector's spectra during reactor off contained no clear features and therefore could not be calibrated. Figure 5.7 are the fast neutron rates in the 0.3 - 6 MeVee range from a detector positioned 38" from the floor throughout reactor-on cycle 468. Once again, this reactor on cycle is the same one as seen in Figures 5.2 and 5.6. The NE213 detector plotted in figure 5.7 was selected as it is the one positionally closest to the detector in Figure 5.2.

As previously highlighted, the main source of fast neutron backgrounds is from cosmic rays. Figure 5.7 shows a definite increase in fast neutron rate after the reactor turns on (9/06/16). This increase is expected to be the result of the NE213 detector triggering on γ -ray pile up in the detectors and interpreted as fast neutrons. The sudden drop in rate seen on 9/14/16 is suspected to be an issue with either the power source or the data acquisition system and not a reactor correlated drop. The rate is relatively consistent throughout the cycle, supporting previous measurements made from the PROSPECT

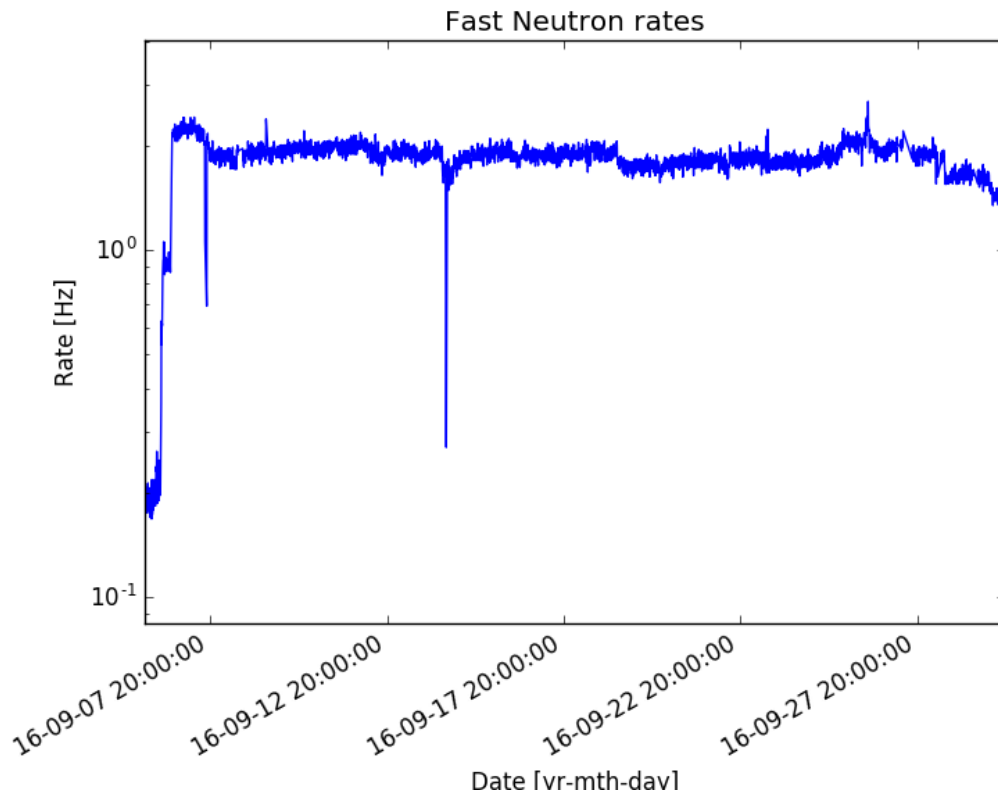


FIGURE 5.7: Measurements taken over a reactor on cycle with NE213 detector 4.

collaboration[37]. The consistency in the rate further supports previous suspicions about HB-3 induced thermal neutron and γ -ray backgrounds. If it was a fast neutron source that was causing the fluctuations seen in figures 5.7 and 5.2 then these same fluctuations would also be observed in the NE213 detectors.

5.4 Spatial Study

As discussed above, we do not expect the background radiation to be uniform or evenly distributed in the experimental area. There should be hot spots of particularly high intensities around the facility and cool spots where the building provides additional shielding, either on purpose or by fortune. A number of measurements in physically different locations across both the experimental and MIF room were conducted in order to understand how the radiation field behaved.

In order to make the measurements at different locations both repeatable and reliable, a coordinate system was contrived and applied through out the area. A centrally located doorway was chosen as the origin. The distance from the origin to a particular measurement point was then carefully measured and recorded. After each measurement, the

location of the measurement was also marked on the floor with its distance from the origin. This process proved extremely useful to ensure the exact same location was used for each iteration of measurements.

The radiation flux was mapped throughout the volume that the PROSPECT detector will occupy. Figure 5.8 outlines where spatial studies were conducted and where the PROSPECT detector will be placed. Unfortunately, the complete volume the PROSPECT detector occupy could not be mapped due to some large storage cabinets. These could not be moved before the final construction that will make space for the PROSPECT detector in the back position.

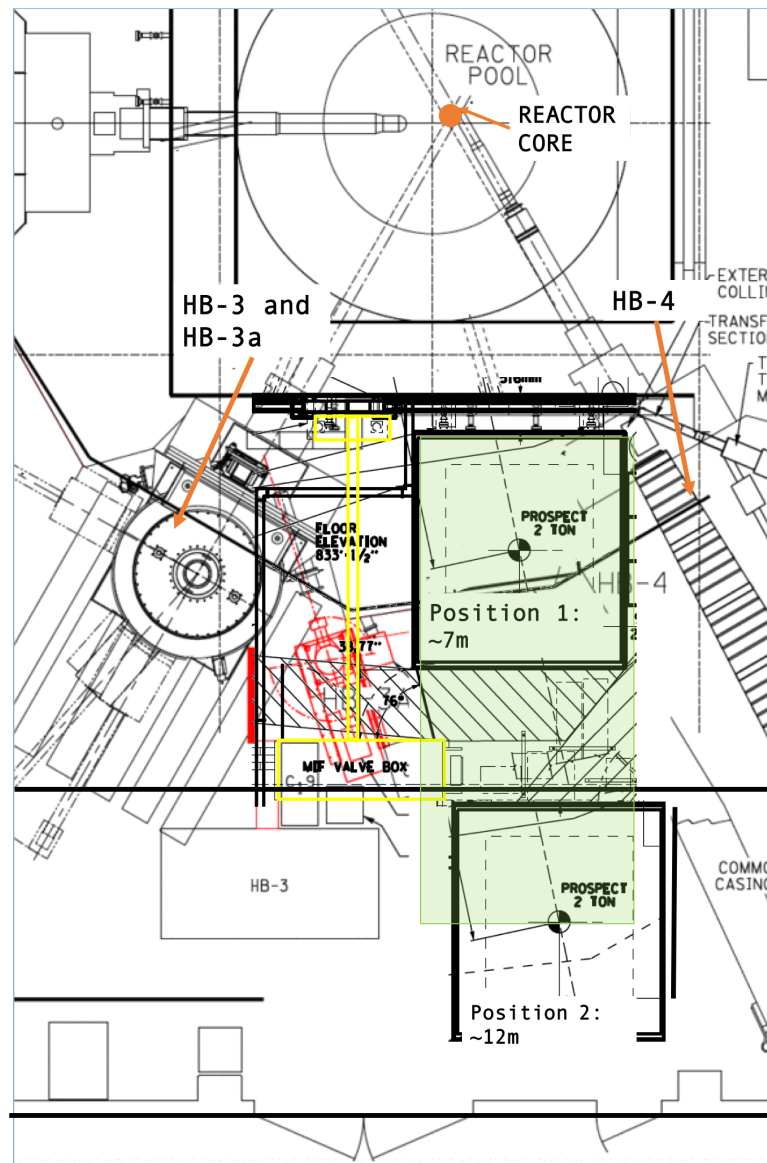


FIGURE 5.8: Diagram of experiment room at HFIR. Black lines represent temporary structures that are currently separating rooms at HFIR. The locations of the PROSPECT detector are displayed at 7m and 12 m from the core. The area shaded in green was the approximate area that DANG measured.

The measurements were compacted into two areas that correspond to the two extreme locations of the PROSPECT detector (7m and 12m from the reactor core[12]). More measurements were conducted perpendicular to the reactor face rather than parallel to the reactor face because the gradient of the fields change more rapidly. The perpendicular gradient therefore had to be more carefully tested, whereas the parallel effects from the beam lines had already been recognised. The measurements for a positional scan were completed over a timescale of a couple of days to minimise the chances of temporal effects distorting the measurements.

5.4.1 NaI Results

As previously mentioned, the NaI(Tl) detectors have known gain shifts. Prior to each positional scan, the NaI(Tl) detectors were calibrated with a ^{137}Cs source. The detectors were positioned at 11", 33", 55" and 81" above the floor with two NaI(Tl) detectors at each of the indicated heights. Two measurements in the positional scans overlap. This provides a check that the rates measured in the two detectors at the same position are similar and comparable.

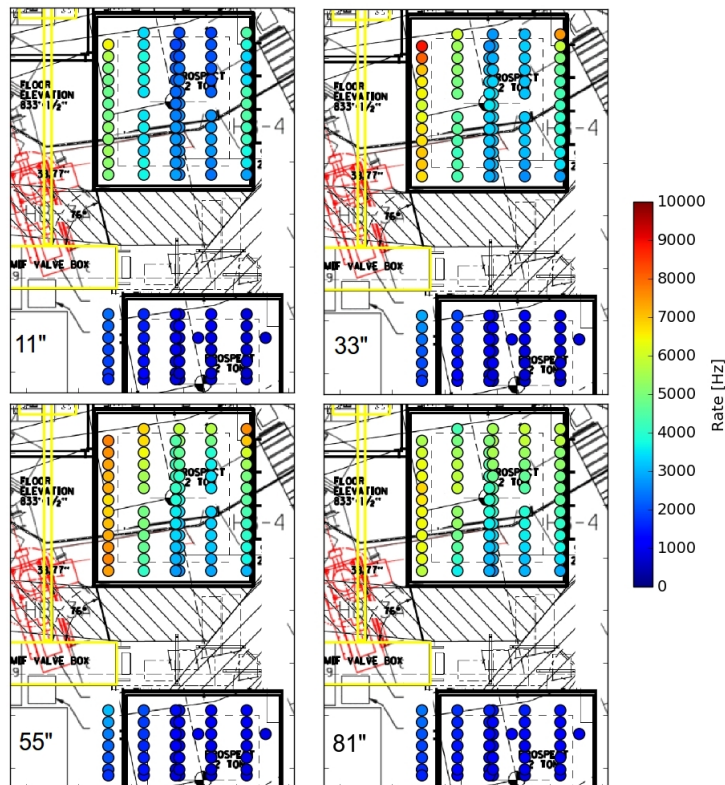


FIGURE 5.9: Positional scan during reactor on with DANG. Rates are for energy range 1-3 MeV.

5.4.1.1 Reactor On Scan

The reactor-on scan was done within the first few days of the reactor period. This was thought to further minimise temporal radiation effects seen in previous measurements[38]. The γ -ray rates in the 1-3 MeV energy region during the reactor-on operation across the mapped area are presented here as Figure 5.9. The detectors located at the top of DANG, 81" from the floor, were highly affected by the radiation given off by the MIF beam line. In contrast, the detectors near the bottom of DANG, 11" from the floor, were more sensitive to the beam lines on the floor below, like HB-4, the cold neutron beam line.

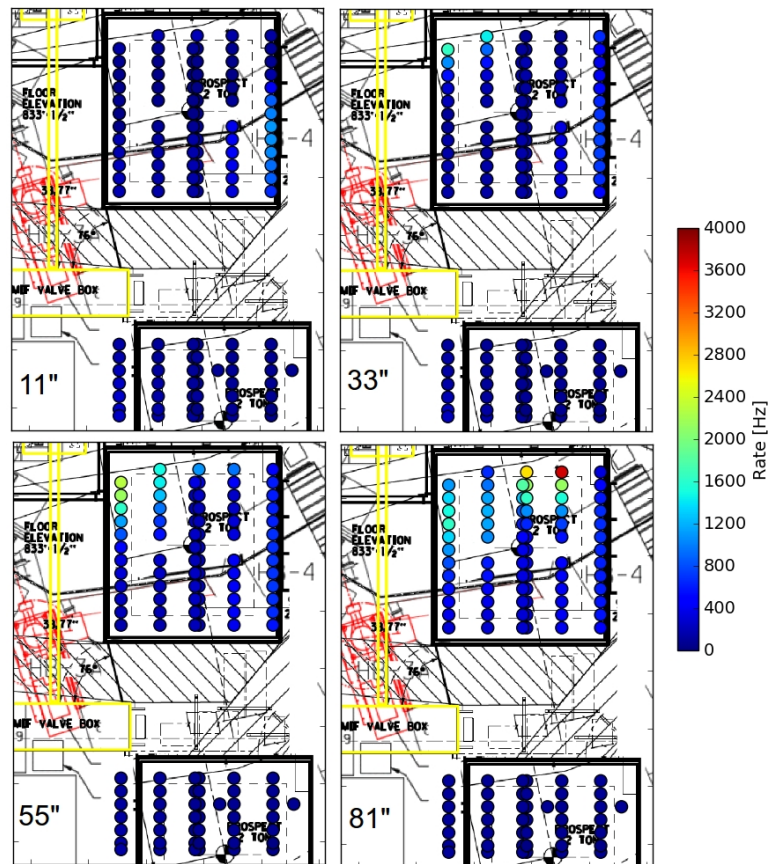


FIGURE 5.10: Positional scan during reactor on with DANG. Rates are for γ -rays observed in the 3-5 MeV energy range.

Figure 5.10 is the same plot as Figure 5.9 but for γ -rays in the 3-5 MeV energy range. In the detector 11" from the floor, the rates in the 3-5 MeV region increase towards neutron beam line HB-4, an effect not observed in the 1-3 MeV range. This is understood to be the result of higher energy γ -rays being produced from neutron capture and then down-scattering[16]. Additionally, there is an increase in rate at heights 33", 55" and 81" for measurements collected nearest the core. This increase is thought to be from valves protruding out from the wall between the room and the reactor core. These valves

connect to the reactor pool where the spent fuel and the reactor core is kept. Again, these γ -rays are likely being produced from neutron-capture in the building's material and then being down-scattered[16].

5.4.1.2 Reactor Off Scan

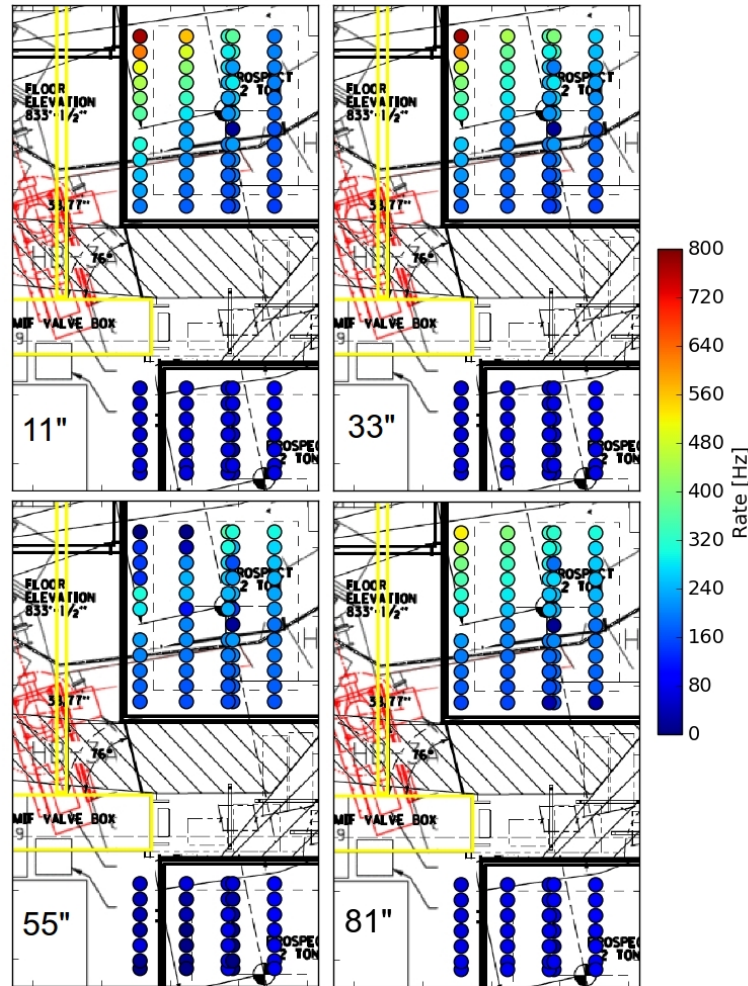


FIGURE 5.11: Positional scan during reactor off with DANG. Rates are for energy range 1-3 MeV.

The reactor off scans were performed the week after the reactor was shut off. The delay was intentional to avoid temporal effects seen when the reactor fuel is removed and other previously correlated reactor operations. The fluctuations in γ -ray rates during reactor shutdown are presented in Figure 5.4. Figure 5.11 shows the 1-3 MeV γ -ray rates in the NaI(Tl) detectors during the reactor-off period.

Comparing the absolute rates between reactor off and on clearly shows the rates are overall much lower during reactor off. Even the hottest areas of the reactor-off scan are lower than the reactor-on scan. A clear hotspot in the reactor-off scan is observed near

the floor in the upper left corner of the measurements. The source of this hotspot has been identified in previous measurements as a vertical column in the floor from beam line HB-3. The higher rates seen in the detectors 81" from the floor are thought to be the result of activated material in the building. There are two potential sources: the MIF entrance box near the ceiling and transport tubing for activated sources during reactor-on. The MIF entrance box is highlighted in yellow in the plot.

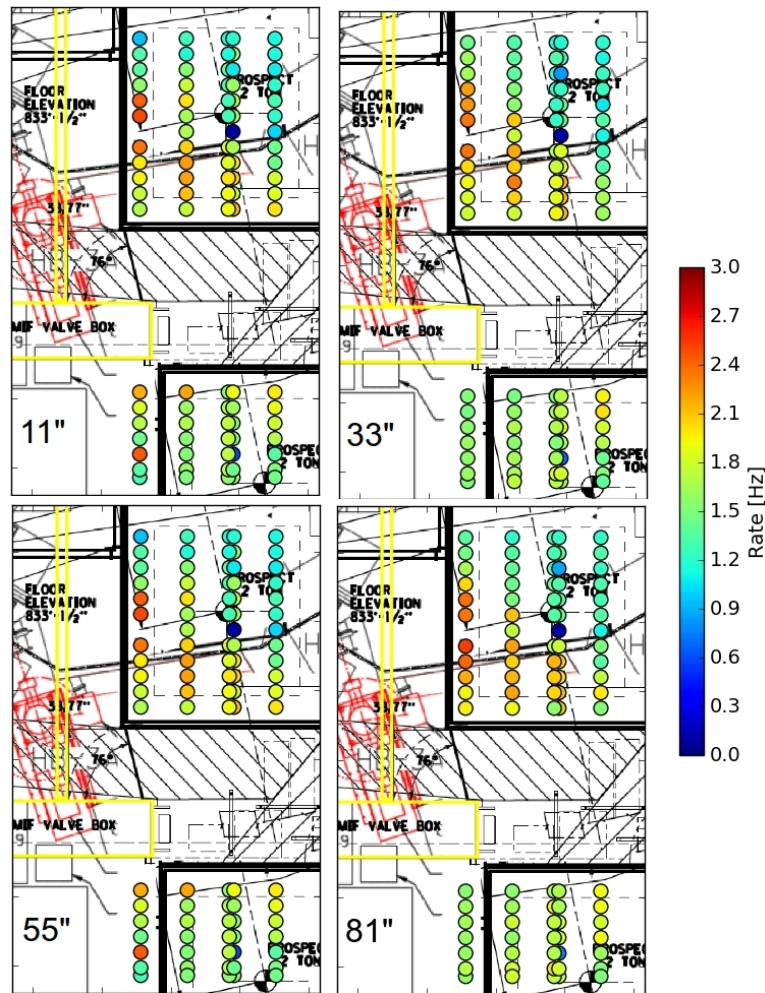


FIGURE 5.12: Positional scan during reactor off with DANG. Rates are for energy range 3-5 MeV.

Figure 5.12 is the same positional scan as figure 5.11 with rates binned on the 3-5 MeV energy range. The rates here are incredibly small compared to both the 1-3 MeV reactor-off rates and the reactor-on rates. Even though the rates double across the room, the differences are minute, ranging from only 1 Hz to 3 Hz. It is therefore difficult to identify a specific source of these changes.

5.4.2 ^3He Results

The ^3He counters are attached at two different heights, in the center of the detector array. The results discussed here were collected during the same positional scans shown in the NaI(Tl) results section. The offset in heights between the two counters is too small to affect the observed rates at various positions as thermal neutrons are understood to be effectively isotropic once they reach the experimental room[12].

5.4.2.1 Reactor On Scan

No hotspots were observed in the rates taken from the ^3He detectors positional scan, as expected. The results of this scan are presented here as Figure 5.13 which displays the rates during the reactor on period.

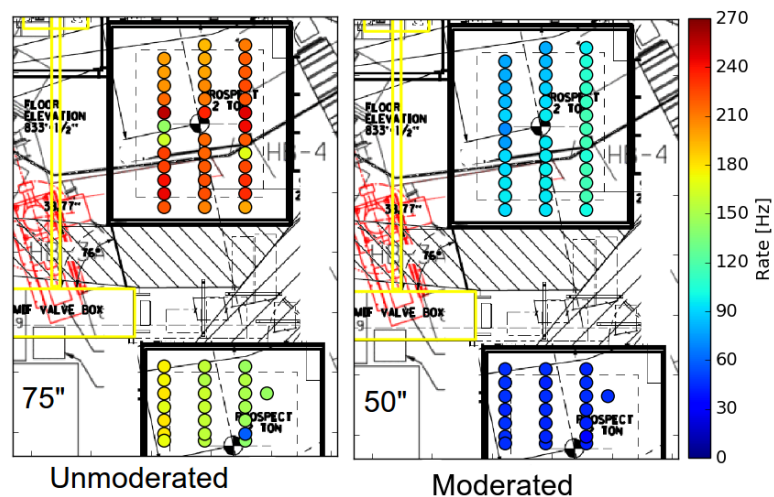


FIGURE 5.13: Positional scan during reactor on with DANG. Rates are for the ^3He detectors.

There is an increase in the rate observed in the moderated ^3He detector towards cold neutron beam line HB-4. This may be the result of neutrons escaping from HB-4. It is believed that faster neutrons are being thermalised in the moderating material around the moderated detector, allowing them to be detected, whereas they are otherwise too high in energy to be observed by the unmoderated detector.

5.4.2.2 Reactor-Off Scan

The main sources of thermal neutrons are all prompt and only observed when the reactor is on. Therefore the rates in the ^3He detectors are very low during a reactor-off period.

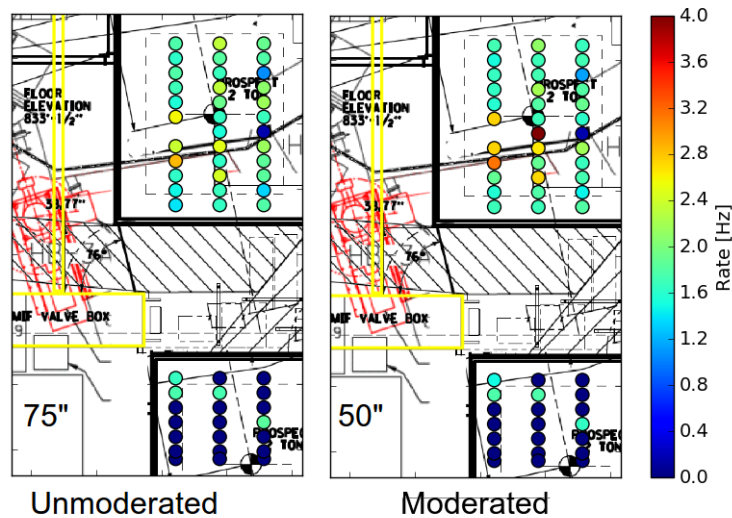


FIGURE 5.14: Positional scan during reactor off with DANG. Rates are for the ^3He detectors.

The results of for these detectors at the various locations through out the experimental hall during the reactor off period are presented here as Figure 5.14.

At first glance, the fluctuations seen in Figure 5.14 appear varied and inconsistent with anything presented so far. With only a few Hz observed in each detector however, these variations are likely to come from either very subtle differences in overburden in the building or a subtle amount of noise in the electronics created from vibrations when the detector array was moved.

5.5 Simulations

Simulations of the NaI(Tl) detector response were conducted in order to de-convolute the spectra into spectral flux. The recorded energy depositions in the detectors were collected into histograms using PROSPECT simulation and analysis tools[38]. The amounting energy "smearing" to match the observed detector resolution was approximated by comparing the simulation of source data to actual data. The sources used in this comparison were ^{60}Co , ^{137}Cs and ^{207}Bi .

The detector response was then simulated for mono-energetic isotropic gammas from 0.1 to 12 MeV in 20 keV increments. Figure 5.15 compares reactor on data, removing the known the ^{41}Ar background, with this simulated data.

The detector response for one of PROSPECT's full 20 litre ^6Li doped test cell was then simulated, generating spectra of γ -ray backgrounds inside the cell during reactor-on.

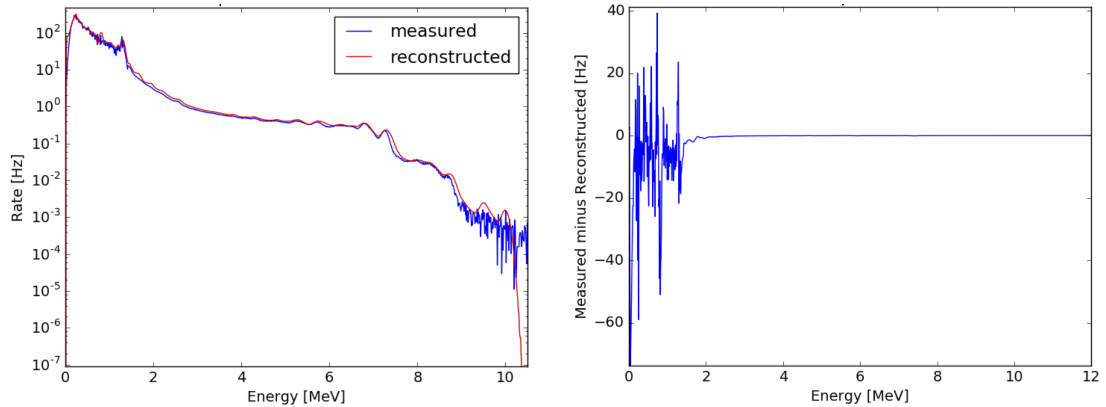


FIGURE 5.15: Left: Data taken from a NaI(Tl) detector during reactor on minus the MIF background component and the reconstructed histogram from the simulation. Right: Differences between the reconstructed and measured energy bins. The total difference is 11.1%

Simulation Type	Total IBD Rate (mHz)	IBD rate, 0.8 - 7.2 MeV (mHz)	Uncertainty, 0.8 - 7.2 MeV (mHz)
Cosmic Neutron	4.98	2.57	0.13
Cosmic muon	0.82	0.41	0.16
Muon accidental	3.71	2.04	0.11
RxOn Gamma acc.	0.01	0.00	N/A

TABLE 5.1: Expected background rates within a 20-litre PROSPECT cell that look like an IBD signal, or have the neutrino signature.

The γ -rays alone observed in the detector will not produce any inverse beta decay (IBD) events, the neutrino detection signature, as a coincident neutron must also be detected. Therefore, the cosmic neutron simulation was used to estimate the neutron capture rate. Reactor correlated neutrons were initially not considered because they are well shielded, hindering their ability to make it into the detector[37]. A summary of the results are shown in the table 5.1.

The ^{41}Ar background radiation from the MIF was simulated separately. The spectrum used was isolated to occur during reactor shutdown. This helps isolate the MIF background source as short-lived neutron-activated materials will decay away before the ^{41}Ar decays away. Figure 5.16 is a comparison of data taken during reactor shutdown and the simulated MIF component approximation.

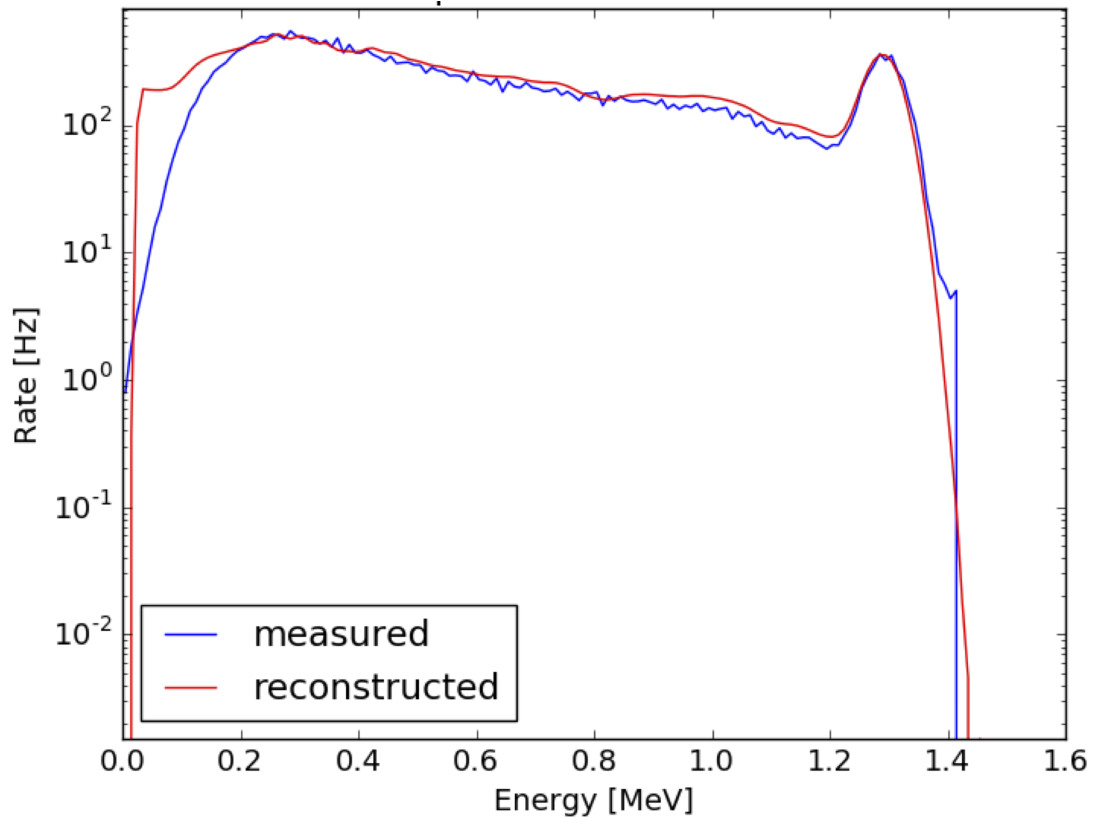


FIGURE 5.16: Measured and isolated MIF background and the approximation of the MIF component from simulation[38]. The shoulder seen in the simulation requires further investigation.

Using this simulation to calculate the IBD rate from the MIF has not currently been completed. The MIF is recognised as a large source of background radiation however, and further studies will be carried out in the future for a more complete understanding[38].

Chapter 6

Outlook and Summary

Research reactors are complex and sophisticated systems. These complexities fully came to light while completing a detailed characterisation of both the spatial and temporal radiation fields at the future PROSPECT site in HFIR. These measurements, taken as part of this characterisation, have highlighted a number of background sources from various reactor operations. The comprehensive understanding of these background sources benefits both the PROSPECT collaboration and future projects wishing to conduct neutrino studies near a reactor core.

6.1 Conclusions of Background Characterisation

The spatial radiation fields fluctuate throughout the volume PROSPECT's detector will occupy, in both the low and high energy regions. These fluctuations were found to be caused by neutron beam lines on the floor below, by valves connecting to the reactor pool, and the MIF experiment. Additional passive shielding that is focused around these sources should help mitigate the flux of γ -rays and neutrons entering the experiment room.

Temporal fluctuations have been seen to heavily affect radiation flux in the experiment room, by as much as $\sim 40\%$. The main source of radiation fluctuations over the reactor-on cycle is from neutron beam line HB-3. The exact functions of the neutron beam line that cause these changes in the neutron flux have yet to be determined. However, with passive shielding already aiming to absorb the large background flux leaking from this beam line, the time dependent fluctuations should be also suppressed.

Apart from spatial and temporal fluctuations, the sheer flux of the background radiation fields seen during reactor-on at close proximity to the reactor core is staggering. These

measurements highlight that the largest and most significant source of background is from the ^{41}Ar gas pumped through the MIF facility. The removal of this source cuts the overall rate in background measurements by $\sim 65\%$. This source was not present during the background characterisation previously performed by the collaboration[37]. Shutting down the MIF facility whilst PROSPECT is operating would greatly reduce background and would be a benefit to the experiment.

Furthermore, DANG has proven to be sensitive to reactor operations. The NaI(Tl) detectors were found to detect spikes in background radiation during reactor operations such as fuel removal and reactor start-up. As well, the ^3He proportional counters count clear fluctuations in rates during specific neutron beam line operations. This measured sensitivity is currently understood to be a useful tool for long term monitoring and future reactor studies.

6.2 Future work

PROSPECT aims to have a constructed and functioning detector by late Summer 2017. As previously mentioned, shielding packages will be installed at HFIR to block background radiation sources observed in current work before the commissioning of the PROSPECT detector. These shielding packages will consist of a lead wall constructed on the wall closest and perpendicular to the reactor. This wall will provide additional shielding to the PROSPECT detector and protection from the valves connecting to the reactor pool. Additional lead shielding will be installed over the vertical column above HB-3. This is where the hotspot was located and a potential source of the temporal fluctuations measured by DANG(Chapter 5).

These shielding packages have been carefully designed to mitigate and suppress background fluctuations seen in the experimental room. The method used in previous background measurements is easily repeatable. DANG is a convenient tool for quick repeatable radiation measurements through a large volume, especially to test the effectiveness of future passive shielding installation in the experiment room. A comparison of the radiation fields before and after the shielding packages are installed will provide important feedback to both the engineers and the simulation group within the collaboration.

The background radiation fields will continue to be monitored after the PROSPECT detector is installed. There have been discussions about installing a smaller version of DANG for long term studies. This version would include one or two NaI(Tl) detectors and a ^3He detector, attached either on the electronics racks or on the detector package itself. A long-term study would provide vital data on how the radiation varies throughout

the room as well as monitor the reactor power output[6]. The background characterisation measurements described will continue to help PROSPECT extract precise reactor antineutrino data to answer some of the questions stumping the physicists of today.

Bibliography

- [1] Philip Morrison. Neutrino Astronomy. *Scientific America*, 207:90–99, 1962.
- [2] L. J. Wen P. Vogel and C. Zhang. Neutrino oscillation studies with reactors. *Nature Communications*, 6(6935), April 2015. URL <https://http://www.nature.com/articles/ncomms7935>.
- [3] M. Cribier. Reactors antineutrino anomalies and searches for sterile neutrinos. *Journal of Physics: Conference Series*, 593:012005, 2015.
- [4] Graphite reactor. "<https://www.ornl.gov/content/graphite-reactor>", 2016.
- [5] Oak Ridge National Laboratory. High flux isotope reactor. "<https://neutrons.ornl.gov/hfir>", 2016.
- [6] Majid jalali, Mohammad Reza Abdi, and Mojtaba Mostajabod davati. Prompt gamma radiation as a new tool to measure reactor power. *Radiation Physics and Chemistry*, 91:19 – 27, 2013. ISSN 0969-806X. doi: <http://dx.doi.org/10.1016/j.radphyschem.2013.05.033>. URL <http://www.sciencedirect.com/science/article/pii/S0969806X13003459>.
- [7] V. F. Sears. Neutron scattering lengths and cross sections. *Neutron News* 3, 3:26, 1992.
- [8] M. García L. E. Herranz, M. P. Kissane. Comparison of lwr and sfr in-containment source term: Similarities and differences. *Progress in Nuclear Energy*, 66:52–60, January 2014.
- [9] F.P. An et al. (Daya Bay Collaboration). Measurement of the reactor antineutrino flux and spectrum at daya bay. *Physics Review Letters*, 116:061801, February 2016. URL <https://arxiv.org/abs/1508.04233>.
- [10] G. Mention, M. Fechner, Th. Lasserre, Th. A. Mueller, D. Lhuillier, M. Cribier, and A. Letourneau. The Reactor Antineutrino Anomaly. *Phys. Rev.*, D83:073006, 2011. doi: 10.1103/PhysRevD.83.073006.

- [11] P. Huber. The 5 mev bump - a nuclear whodunit mystery. *arXiv*, September 2016. URL <https://arxiv.org/abs/1609.03910>.
- [12] J. Ashenfelter et al. (PROSPECT Collaboration). The prospect physics program. *Journal of Physics G*, 43(11), October 2016. URL <http://iopscience.iop.org/article/10.1088/0954-3899/43/11/113001/meta>.
- [13] J. A. Bucholz. Source terms for hfir beam tube shielding analyses, and a complete shielding analysis of the hb-3 tube. Technical report, Oak Ridge National Laboratory, July 2000. URL <http://www.sciencedirect.com/science/article/pii/S016890020800853X>.
- [14] Gordon Gilmore. *Practical Gamma-ray Spectrometry*. John Wiley and Sons, Warrington, UK, 2008.
- [15] Nuclear Power. Interaction of gamma radiation with matter. "<http://www.nuclear-power.net/nuclear-power/reactor-physics/interaction-radiation-matter/interaction-gamma-radiation-matter/>", 2016.
- [16] Glenn F. Knoll. *Radiation Detection and Measurement*. Jon Wiley and Sons, Ann Arbor, Michigan, 2010.
- [17] F.G.A. Quarati, P. Dorenbos, J. van der Biezen, Alan Owens, M. Selle, L. Parthier, and P. Schotanus. Scintillation and detection characteristics of high-sensitivity cebr3 gamma-ray spectrometers. *Nuclear Instruments and Methods in Physics Research Section A: Accelerators, Spectrometers, Detectors and Associated Equipment*, 729:596 – 604, 2013. ISSN 0168-9002. doi: <http://dx.doi.org/10.1016/j.nima.2013.08.005>. URL <http://www.sciencedirect.com/science/article/pii/S0168900213011297>.
- [18] *NEUTRON/GAMMA PSD LIQUID SCINTILLATOR EJ-301, EJ-309*. ELJEN Technology, 2016. URL http://www.eljentechnology.com/images/products/data_sheets/EJ-301_EJ-309.pdf.
- [19] G. Nebbiab L. Stevanatoa G. Viestia S. Petruccic C. Tintoric D. Cestera, M. Lunnardona. Pulse shape discrimination with fast digitizers. *Nuclear Instruments and Methods in Physics Research Section A*, 748(1):33–38, June 2014. URL <http://www.sciencedirect.com/science/article/pii/S016890021400196X>.
- [20] *Photomultiplier Tubes: Basics and Applications*. Saint-Gobain, 2016. URL http://www.crystals.saint-gobain.com/sites/imdf.crystals.com/files/documents/proportional-counters-data-sheet_69732.pdf.

- [21] L.D.P. King and L. Goldstein. The total cross section of the he, nucleus for slow neutrons*. *Physical Review*, 75(9):1366–1369, May 1949. URL <http://journals.aps.org/pr/pdf/10.1103/PhysRev.75.1366>.
- [22] V. Radeka. Gas-based thermal neutron detectors. DOE BES Neutron & Photon Detector Workshop, 2012.
- [23] *User Manual VX1730*. CAEN, 2016. URL <http://www.caen.it/csite/CaenProd.jsp?parent=11&idmod=780>.
- [24] *9266B series data sheet*. ET Enterprises, 2010. URL <https://my.et-enterprises.com/pdf/9266B.pdf>. Issue 10.
- [25] *Model 276L Power Photomultiplier Base*. ORTEC, 2013. URL <http://www.ortec-online.com/Service-Support/Library/Manuals.aspx>. Rev. 3.
- [26] ET Enterprises. *Understanding Photomultipliers*. ET Enterprises, 2011. URL <http://www.et-enterprises.com/photomultipliers/understanding-photomultipliers>.
- [27] D. Akimov et al. (COHERENT Collaboration). The coherent experiment at the spallation neutron source. *arXiv*, September 2015. URL <https://arxiv.org/abs/1509.08702>.
- [28] J. T. Matta. Private Communication. DANG DAQ operation, 2016.
- [29] *Photomultiplier Tubes Catalogue*. PHOTONIS, 2007. URL <https://hallcweb.jlab.org/DocDB/0008/000809/001/PhotonisCatalog.pdf>. Page 56.
- [30] *Photonis Voltage Dividers*. Photonis, accessed: 2016. URL goo.gl/0xdknYf.
- [31] J. Nyberg P.-A. Sderstrm and R. Wolters. Digital pulse-shape discrimination of fast neutrons and rays. *Nuclear Instruments and Methods in Physics Research Section A*, 594:79–89, August 2008. URL <http://www.sciencedirect.com/science/article/pii/S016890020800853X>.
- [32] Veljko Radeka. Gas-based thermal neutron detectors. unpublished, 2012. URL <https://goo.gl/0BMgbf>.
- [33] Saint-Gobain. *Helium-3 Proportional Counters*. Saint-Gobain, 2016. URL http://www.crystals.saint-gobain.com/sites/imdf.crystals.com/files/documents/proportional-counters-data-sheet_69732.pdf.
- [34] Wiener Power Electronics. *MPOD Crate*, 2016. URL <http://www.wiener-d.com/sc/power-supplies/mpod--lvhv/mpod-crate.html>.

-
- [35] Wiener Power Electronics. *6U VME64x 395-x Mini*, 2016. URL <http://www.wiener-d.com/sc/powerd-crates/vme64-x/6u-vme64x-395-x-mini.html>.
- [36] Prospect - a precision oscillation and spectrum experiment. "<http://prospect.yale.edu/>", 2016.
- [37] J. Ashenfelter et al. (PROSPECT Collaboration). Background radiation measurements at high power research reactors. *Nuclear Instruments and Methods in Physics Research Section A*, 806(11):401–419, January 2016. URL <http://www.sciencedirect.com/science/article/pii/S0168900215012309>.
- [38] B.A. Heffron. Characterization of Reactor Background Radiation at HFIR for the PROSPECT Experiment. Master's thesis for University of Tennessee, 2017.
- [39] Oak Ridge National Laboratory. Hb-3 users log, 2016.